Desalination 615 (2025) 119312

Contents lists available at ScienceDirect

Desalination

journal homepage: www.elsevier.com/locate/desal

# Ammonium removal from water using flow capacitive deionization with MgO-modified biochar derived from orange peels

Gabriel Mwalusambo [a,b], Bethwel Tarus [c], Joyce Elisadiki [d], Moon Son [e], Hoo Hugo Kim [e], Yusufu A.C. Jande [a,f], Tusekile Alfredy [a,f,*]

[a] Department of Materials and Energy Sciences and Engineering, Nelson Mandela African Institution of Science and Technology, P.O. Box 447, Arusha, Tanzania
[b] Department of Process and Energy Engineering, Mwalimu Nyerere University of Agriculture and Technology (Butiama-HQ), P.O. Box 976, Musoma, Mara, Tanzania
[c] Department of Manufacturing, Industrial and Textile Engineering, Moi University, P.O. Box 3900, 30100 Eldoret, Kenya
[d] Department of Physics, College of Natural and Mathematical Sciences, University of Dodoma, P.O. Box 338, Dodoma, Tanzania
[e] Center for Water Cycle Research, Korea Institute of Science and Technology, 5 Hwarang-ro 14-gil, Seongbuk-gu, Seoul 02792, Republic of Korea
[f] Water Infrastructure and Sustainable Energy Futures (WISE-Futures) African Centre of Excellence, The Nelson Mandela African Institution of Science and Technology, Nelson Mandela Road, Tengeru, P.O. Box 9124, Nelson Mandela, Arusha, Tanzania

## HIGHLIGHTS

- High ammonium ($NH_4^+$) levels in water sources affect ecosystems.
- The flow capacitive deionization (FCDI) method effectively removes $NH_4^+$ from water.
- Magnesium oxide modified biochar makes FCDI even better at removing $NH_4^+$.
- Achieved 86.7 % $NH_4^+$ removal efficiency with a rate of 17.3 mg $m^{-2}$ $min^{-1}$
- Surface modification of biochar with MgO minimizes energy consumption.

## GRAPHICAL ABSTRACT

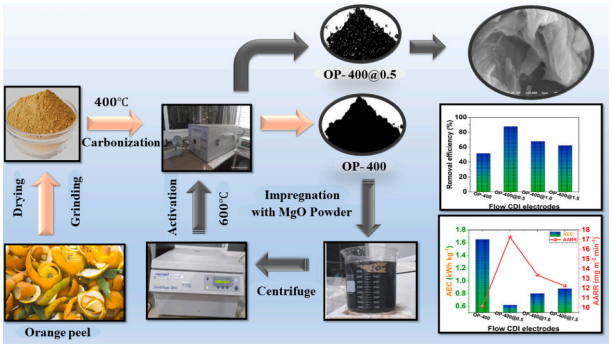


## ARTICLE INFO

*Keywords:*
Ammonium removal
Biochar
FCDI
Flow-electrodes

## ABSTRACT

Ammonium ($NH_4^+$) in water presents substantial environmental challenges, such as eutrophication and toxicity that necessitate effective removal strategies. This study developed flow electrodes using biochar obtained from orange peels for the removal of $NH_4^+$ from water through flow capacitive deionization (FCDI). The biochar was prepared through carbonization and modification with MgO at varying ratios using the co-precipitation method. The modified biochar exhibited high hydrophilicity and demonstrated a specific capacitance of 238 F $g^{-1}$. The FCDI process was optimized at an applied voltage of 1.2 V, an electrode flow rate of 10 mL $min^{-1}$ and a 2.5 wt% carbon content in the flow electrode. The modified flow electrodes showed effective performance, attaining an average $NH_4^+$ removal rate of 17.3 mg $m^{-2}$ $min^{-1}$, removal efficiency of 86.7 % and retention of 91.3 % after 30 cycles. Notably, the modified MgO flow electrode resulted in approximately 62 % reduction in energy consumption during electrosorption compared to pristine biochar, indicating advantages emanating from reduced

* Corresponding author at: Department of Materials and Energy Sciences and Engineering, Nelson Mandela African Institution of Science and Technology, P.O. Box 447, Arusha, Tanzania.
*E-mail addresses:* mwalusambog@nm-aist.ac.tz (G. Mwalusambo), joyce.lyimo2@udom.ac.tz (J. Elisadiki), tusekile.alfredy@nm-aist.ac.tz (T. Alfredy).

https://doi.org/10.1016/j.desal.2025.119312
Received 7 June 2025; Received in revised form 31 July 2025; Accepted 13 August 2025
Available online 14 August 2025

solution and charge transfer resistances. Experiments with simulated municipal wastewater confirmed the modified electrode's superior ability, consistent stability over multiple cycles, and selectivity in $NH_4^+$ removal. This study highlights the efficacy of the developed flow electrodes for FCDI systems, offering a straightforward electrode synthesis method and effective $NH_4^+$ removal.

## 1. Introduction

Water contamination by nutrients such as ammonium ($NH_4^+$) poses a significant risk to water security, public health, and ecosystems. Industrial effluents, municipal discharges, and agricultural runoff inevitably contribute to excess $NH_4^+$ in water bodies, this leads to reduced water quality, eutrophication, and disruption of aquatic ecosystems [1–4]. The permissible limit of $NH_4^+$ level in drinking water is 1.5 mg $L^{-1}$, as set by the World Health Organization (WHO), and 1 mg $L^{-1}$, as set by the Tanzania Bureau of Standards (TBS) [5].

Conventional $NH_4^+$ removal techniques such as air stripping, struvite precipitation, reverse osmosis, and ion exchange have achieved commercial success but suffer challenges, which include operational complexity, high energy consumption, high maintenance, and need for chemical additives, which can cause secondary pollution [6,7]. Thus, there is increasing interest in advancing alternative technologies such as capacitive deionization (CDI), which promises sustainability, is environmentally friendly, and has low energy consumption. CDI operates by capturing ionic species in water using high-surface-area porous electrodes [8–10]. However, extensive use of conventional CDI is limited by drawbacks such as low charge efficiency, short cycle operation, and reduced performance in concentrated feed solutions [11,12]. Recent advances have led to development of flowable electrode capacitive deionization (FCDI), which enables better charge transfer efficiencies and continuous operation [13,14]. FCDI employs a suspension of conductive porous particles as flowable electrodes that circulate through channels in the current collectors, while the feed solution is simultaneously passed between the electrodes separated by ion exchange membranes (IEMs) [15,16]. Ions from the feed solution migrate across the IEMs into the electrode chambers, where they are adsorbed under the influence of an electric field. The flow electrode then transports and releases the ions for regeneration [14,17].

Various materials such as activated carbon, carbon black, carbon nanotubes, and carbon nanofibers have been used as flow electrodes in FCDI for $NH_4^+$ removal due to their good electrical conductivity, high specific surface area, and flowability [18–20]. However, most of these materials face challenges related to their regeneration, cost, and limited surface functionalities [21,22]. Additionally, activated carbon, which is commercially available, is derived from coal, a non-renewable resource. Also, organic electrode materials have rapidly emerged as next-generation CDI electrodes, providing enhanced salt removal capacities and tunable electrochemical properties, along with potential environmental benefits compared to conventional carbon-based materials. However, challenges related to electrical conductivity, long-term stability, and scalable manufacturing still need to be addressed [23,24]. This has sparked interest in renewable, carbon-rich materials derived from widely available biomass wastes, offering a reduced environmental impact in addition to high porosity and favorable surface chemistry [25,26]. Precursors such as agricultural, marine, and forestry wastes have been utilized, demonstrating sustainable solutions for water desalination and ion removal [9,19,27].

In this study, orange peels have been selected since they are abundant organic waste and an excellent biochar resource [28,29]. Orange peel-derived biochar has shown potential for the electrochemical removal of contaminants, such as dyes and heavy metals, from wastewater due to its inherent porosity and surface functionality [30–32]. Nevertheless, some degree of surface modification is typically required to enhance the physicochemical properties of biochar and improve its electrosorption capacity [33,34]. The impregnation of biochar with metal oxides has been shown to enhance key features essential for contaminant removal via electrochemical means [30,32,35–37]. For instance, magnesium oxide-modified carbons derived from various biomass sources, including sewage sludge, have demonstrated remarkable removal capacities for $Cu^{2+}$, $Pb^{2+}$, $PO_4^{3-}$, $Cd^{2+}$, and $NH_4^+$ from water [34,38,39].

In this study, biochar derived from orange-peel wastes was prepared and modified with MgO for use as flow electrodes with enhanced $NH_4^+$ removal capacity through FCDI. The performance of the developed flow electrodes was evaluated in terms of the average $NH_4^+$ removal rate, removal efficiency, desorption efficiency, and energy consumption. In general, this study highlights the efficiency of modified biochar-based flow electrodes in FCDI systems, offering a low-cost electrode synthesis approach and effective nutrient removal from water.

## 2. Materials and methods

### 2.1. Materials

Orange peels were gathered from local markets in Arusha. Magnesium oxide powder (MgO) and hydrochloric acid (HCl) were purchased from Sigma-Aldrich. Sodium hydroxide (NaOH), Sodium chloride (NaCl), Calcium chloride ($CaCl_2$), and ammonium sulfate ($(NH_4)_2SO_4$) were sourced from LOBA CHEMIE PVT LTD. Carbon black and polyvinylidene fluoride (PVDF) were purchased from Shandong Richnow Chemical Company. Deionized water (DI) was purchased from CHEMLANA SPRINGS. Since these chemicals were of analytical grade, they were used as received without modification.

### 2.2. Preparation of pristine and modified biochar from orange peel

Orange peels were washed and rinsed several times to remove impurities and dried overnight in an oven at 80°C. The dried peels were then ground to produce orange peel powder (OP), which was sieved using a British Standard sieve with a mesh size of 90 μm (number 170). Orange peel-derived biochar was prepared (Fig. 1) by thermal treatment of OP in a tube furnace at 400°C for 120 min at 5°C $min^{-1}$ heating rate under controlled conditions $N_2$ gas as adopted from Zhengfeng et al. [32]. The biochar sample obtained was labeled as OP-400. Impregnation of the biochar with MgO was conducted using the co-precipitation method at a MgO:OP-400 mixing ratio of 0.5:1, 1.0:1, and 1.5:1 in deionized water (DI). The mixture was stirred for 30 min and left to stand for 120 min, followed by centrifugation to obtain the precipitate, which was then dried overnight at 60 °C. Activation of the dried precipitate was conducted in a tube furnace at 600 °C for 120 min, with a heating rate of 5 °C $min^{-1}$, and controlled $N_2$ gas purging at a rate of 18 mL $min^{-1}$ as per the works of Li et al. [3] and Heo and Park [40]. The MgO-modified sample was washed several times with DI water to remove impurities until the conductivity became less than 10 μS $cm^{-1}$, then dried overnight in a 60 °C oven, ground, and labeled OP-400@A, where A stands for MgO powder ratio.

### 2.3. Characterization of materials

The surface morphology of the orange peel-derived biochar was analyzed using a scanning electron microscope (SEM) (JSM-IT200 InTouchScope). The specific surface area was determined using the

Brunauer-Emmett-Teller (BET) method, and the non-local density function method (NLDFT) was employed to determine the pore size distribution (Quantachrome, 1994-2013), operating at 77.35 K with a relative pressure of 0.9887. The sample was initially outgassed at 300°C in a vacuum. The elemental composition and valence states of each element were analyzed by X-ray photoelectron spectroscopy (XPS) (PHI 5000 VersaProbe (Ulvac-PHI, Japan)). Atomic structure was also determined using X-ray diffraction (XRD) (TERRA-607). The degree of biochar disorder was determined by Raman spectroscopy (RWF20250328). The hydrophilicity of the biochar was assessed using a Goniometer analyzer (L 2004A-0388). Thermogravimetry (TGA) was employed to evaluate the thermal stability and composition of the materials. Finally, a Fourier Transform Infrared Spectrometer (FTIR) was used to identify the functional groups on the surface of the material (Shimadzu IRSpirit-A224159).

### 2.4. Electrochemical measurements

The electrochemical properties of biochar were determined by cyclic voltammetry (CV), Galvanostatic charging-discharging (GCD), and electrochemical impedance spectroscopy (EIS) using a potentiostat-galvanostat (PGSTAT204, AUT50663 Metrohm) as the working station. Molar solutions of $(NH_4)_2SO_4$, NaCl, and $CaCl_2$ were used as electrolytes for CV, GCD, and EIS tests. Active material served as a working electrode, a platinum counter electrode against Ag/AgCl (for NaCl, $CaCl_2$), and Hg/HgO (for $(NH_4)_2SO_4$) in a three-electrode system. The working electrode was fabricated using the procedure described by Enock et al. [41], which involved compressing approximately 5 mg of active material, polyvinylidene difluoride (PVDF), and carbon black in a mass ratio of 80:10:10 onto two pieces of nickel foam. These electrodes were designated as OP-400 and OP-400@0.5. The EIS test was conducted within a frequency range of 0.01 to 100 kHz, using an amplitude of 10 mV. The CV test was set at the potential range of −1.0–0.0 V for OP-400 and −0.1–1.0 V for OP-400@0.5 while varying scan rates as 100, 80, 60, 40, 20, and 5 $mVs^{-1}$. The specific capacitance (F $g^{-1}$) from CV tests were determined using Eq. (1), and for GCD, it was determined by using Eq. (2).

$$C = \int_{v_i}^{v_f} \frac{I}{rm\Delta V} dv \quad (1)$$

where I (A) is the response current, r ($Vs^{-1}$) is the scanning rate potential, ΔV (V) is the potential window employed, and m (g) is the mass of active material in the electrode.

$$C = \frac{I\Delta t}{m\Delta V} \quad (2)$$

$$\tau_0 = {}^{1}/_{f_0} \quad (3)$$

where I (A) is the current, Δt (s) is the discharging time, m (g) is the mass of active material, ΔV (V) is the potential window applied, $\tau_0$ (s) is the time constant, and $f_0$ (Hz) is the characteristic frequency at −45° phase angle.

### 2.5. Preparation of flow CDI electrode material and its operation

The $NH_4^+$ Removal from water was accomplished using a lab-scale prototype FCDI system (Fig. 2), with dimensions of 80 mm × 80 mm × 5 mm. The two opposite stainless steel current collectors (in the cathode and anode) are engraved to create electrode flow channels. Channels are 40 mm long, 36 mm wide, and 2.5 mm deep. The prototype has 17 channel columns that provide an effective contact area of 14.4 $cm^2$ between the flow electrode and the ion exchange membranes (IEM). Unmodified and MgO-modified biochar electrodes flowed through the semicircular channels without a blocking mechanism. A rubber gasket prevented short-circuiting and leakage, allowing for the recirculation of the feed solution by separating the ion exchange membranes. Two end plates made of polyvinyl chloride kept everything together. The $NH_4^+$ removal was conducted using an FCDI cell in short-circuited closed cycle (SCC) mode. The flow electrode was stirred continuously throughout the experiment to secure homogeneity and enhance charge cancellation. Fig. 2b depicts the FCDI flow setup. 50 mL of $NH_4^+$ solution as feed solution circulated continuously in the space chamber, and 50 mL of flow electrodes were distributed equally to the cathode and anode chambers during experiments. The operating

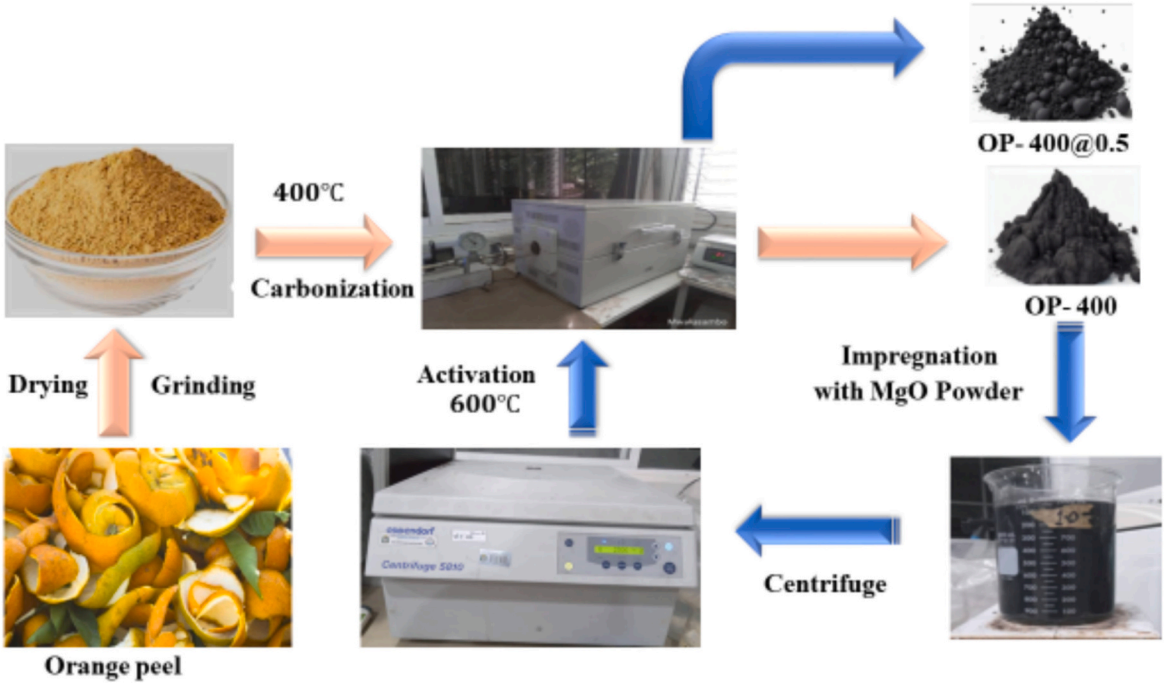


**Fig. 1.** Orange peel-derived biochar preparation process.

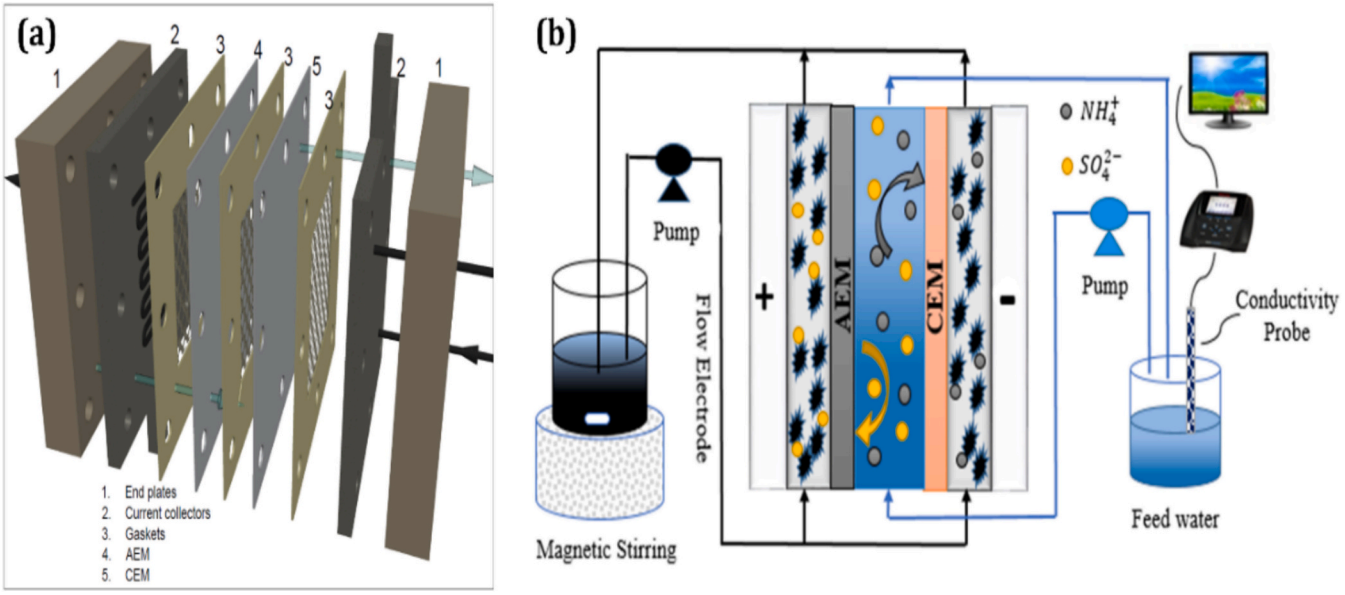


**Fig. 2.** (a) FCDI cell and (b) FCDI flow setup.

conditions for all experiments were a pH of 6, a flow rate of 10 mL $min^{-1}$, and a contact time of 120 min. A voltage of 1.2 V was applied to avoid water electrolysis faradaic reactions as adopted from Zhang et al. [42] and Li et al. [2,3]. Due to the smaller-sized FCDI cell, 2.5 wt% carbon content was used to prevent electrode flow clogging, as also reported by Saif et al. [43]. To avoid scaling up the FCDI system the pipes were instantly washed with DI water after each experimental trial to remove clogged particles. During the experiments, the conductivity, response current, and pH were continuously recorded every 5 s using a conductivity meter (ORION STAR A111, Thermo Scientific). After each experiment, the FCDI cell was thoroughly cleaned with DI water.

The concentration of $NH_4^+$ was determined using the calibration curve correlation with conductivity, as depicted in Fig. 3. Therefore, the initial and final concentration of $NH_4^+$ was determined as a function of conductivity. The concentration of $NH_4^+$ in the flow electrode filtrate was determined using the Nessler method on a spectrophotometer (Hach, DR 1900). Determination of $Na^+$ concentration was via a flame photometer (Jenway, PFP 7), while $Ca^{2+}$ concentration was measured using the EDTA titration method (Digital titrator, Brand (Titrette)). The FCDI performance was determined in terms of $NH_4^+$ removal efficiency (RE), selectivity, desorption efficiency (DE), adsorption energy consumption (AEC) [13], and average ammonium removal rate (AARR) [2,3].

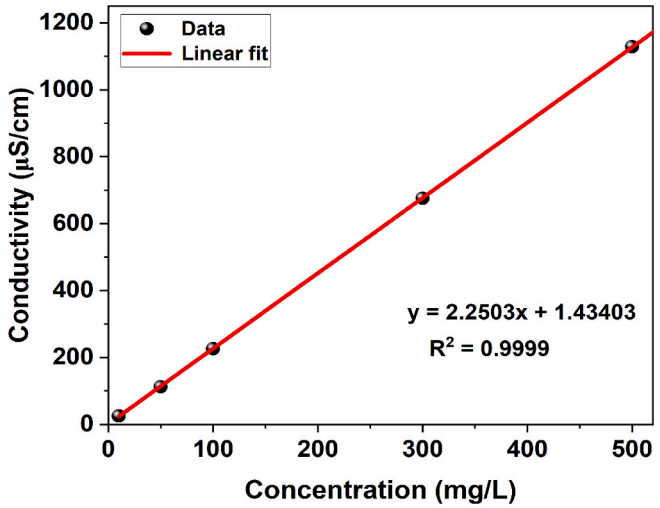


**Fig. 3.** Conductivity and concentration calibration curve.

$$RE = \frac{C_0 - C_t}{C_0} \times 100\% \quad (4)$$

$$Selectivity = \frac{RE_{(NH_4^+)_i}}{RE_i} \quad (5)$$

where $C_0$ and $C_t$ denote the initial and equilibrium concentrations of the feed solution (mg $L^{-1}$), $RE_i$ for the removal efficiency of selected co-existing ions, and $RE_{(NH_4^+)_i}$ represents the RE of $NH_4^+$ ions from water along with respective co-existing ions.

$$AARR\ (mg\ m^{-2}\ min^{-1}) = \frac{(C_o - C_t)\ V_f \times M}{A \times t} \quad (6)$$

$$AEC\ (kWh\ kg^{-1}) = \frac{V \int_0^t Idt}{(C_0 - C_t)V_f} \times 10^3 \quad (7)$$

$$DE = \frac{C_e V_e}{(C_0 - C_t)V_f} \times 100\% \quad (8)$$

where $C_e$ is the final concentration in the flow electrode (mg $L^{-1}$), $V_e$ is the volume of flow electrode suspension (L), V is the applied voltage, $V_f$ is the volume of the feed solution (L), M is the molar mass of $NH_4^+$ (18 g $mol^{-1}$), A is the contact area between the feed solution and IEMs, and t is the FCDI charging time (min).

## 3. Results and discussions

### 3.1. Characterization of materials

The surface morphology and effects of modification on the produced materials were analyzed using SEM (Fig. 4a–d), as also confirmed by SEM-EDX (Figs. S3–S4) in Supplementary information. The SEM micrograph of OP-400 (Fig. 4a) revealed an irregular, flaky structure with folds, wrinkles, limited pores, and stacked sheets. In Fig. 4b, OP-400@0.5 displayed increased layering, enhanced pores, and a modified surface texture, as observed by Bediako et al. [30]. The observation aligns with the incorporation of MgO onto the OP-400@0.5 electrode surface of 1.44 wt% compared to 0.22 wt% of the OP-400 electrode

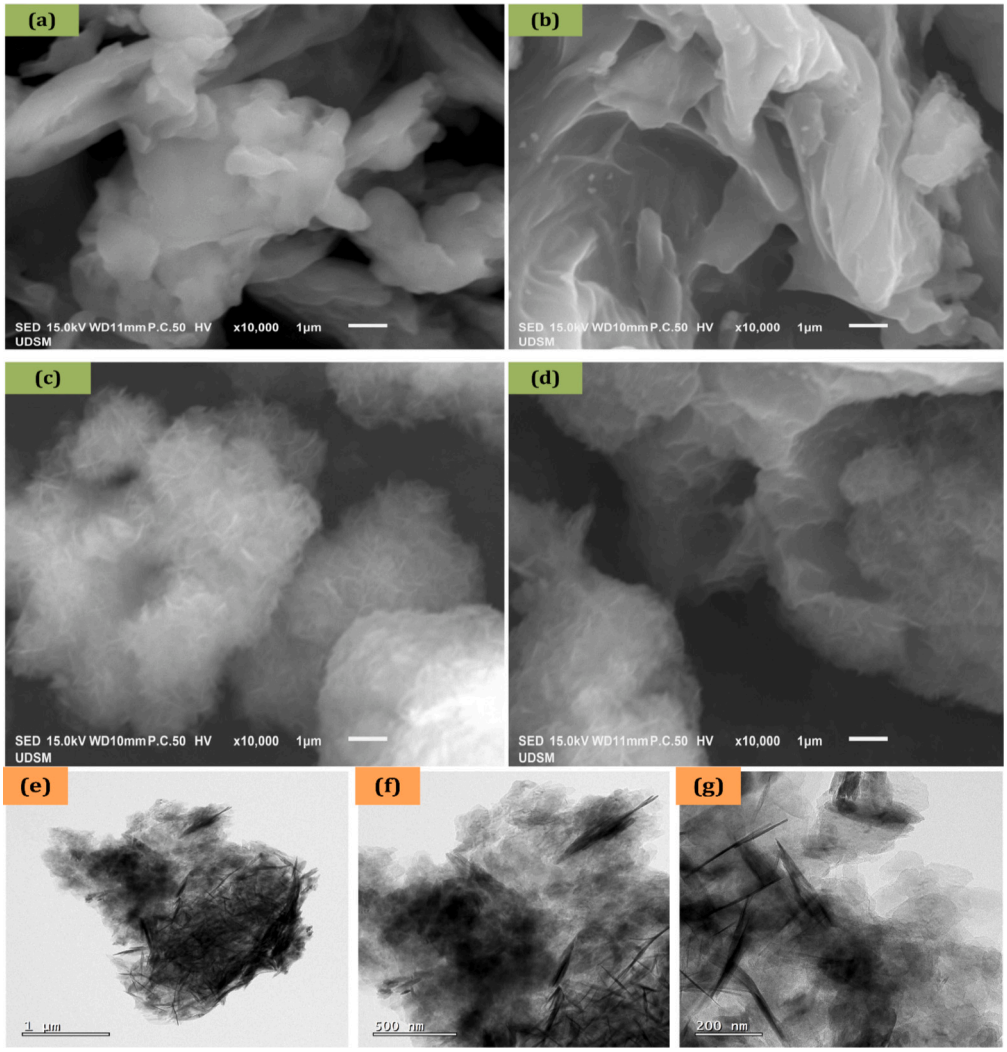


**Fig. 4.** SEM micrograph of (a) OP-400, (b) OP-400@0.5, (c) OP-400@1.0, and (d) OP-400@1.5, TEM images of OP-400@0.5 at (e) 1 μm, (f) 500 nm, and (g) 200 nm resolutions.

(Fig. S3a), which strengthens the carbon structure [44]. Fig. 4c shows OP-400@1.0 with a fluffy, cotton-like structure that was porous and rough, featuring small fibers and nodules. OP-400@1.5 (Fig. 4d) appeared clustered and porous with large, defined three-dimensional networks. The development of fluffy, cloud-like structures in OP-400@1.0 and OP-400@1.5 suggested that MgO modification created nucleation sites for new structures during activation. The structural change could be attributed to the increased MgO on the biochar surface, as evidenced by EDX elemental mapping, showing 4.52 wt% in OP-400@1.0 and 39.64 wt% in OP-400@1.5 (Fig. S3b). This appearance is not solely a result of a carbon structure, but rather the interaction between the carbon matrix and the dispersed MgO nanoparticles, which disrupts the original carbon structure and increases surface roughness and porosity [45–47]. Nanosized MgO exhibits a remarkable ability to infiltrate and hot-extrude into the pores and fissures of biochar [48].

An increase in porosity was observed, as detailed in Table 1. Before MgO modification, OP-400 (1.83 nm) exhibited limited pore development. However, a significant morphological transformation was observed after modification, with increased layering and cavity enlargement in OP-400@0.5 (1.86 nm). Further improvements led to more pronounced structural variations, including the formation of fluffy, cloud-like structures in OP-400@1.0 (4.38 nm) and OP-400@1.5 (4.53 nm) biochar materials. These findings suggest that MgO activation enhances biochar porosity through infiltration and extrusion into pores and fissures (Figs. S3b, S4a–b).

**Table 1**
Porosity properties of materials.

| Sample | Specific surface area ($m^2\ g^{-1}$) | Average pore size (nm) | Pore volume ($cm^3\ g^{-1}$) |
|---|---|---|---|
| OP-400 | 460.27 | 1.82 | 0.362 |
| OP-400@0.5 | 389.56 | 1.86 | 0.418 |
| OP-400@1.0 | 329.36 | 4.38 | 0.612 |
| OP-400@1.5 | 270.14 | 4.53 | 0.722 |

On the other hand, OP-400@0.5 biochar displayed enhanced porosity, presenting more active sites necessary for effective $NH_4^+$ electrosorption. Biochar morphology, crystal structures, and defects were analyzed using TEM (Fig. 4e–f) at resolutions of 1 μm, 500 nm, and 200 nm. The images displayed two regions: less dense areas for amorphous biochar and well-defined needle-like crystallite structures (MgO) [49]. The integrated crystals formed interconnected networks within the biochar structures, promoting the creation of essential interfacial boundaries for Mg-O-C bond formation and supporting oxygen-containing functional groups (-OH, C═O, C—O) [50,51]. The irregular

edges of the needle-like structures provided reactive surface chemistry for the attachment of oxygen-containing functional groups, enhancing adsorption capacity, stability, and reactivity through reinforced structures and additional functional groups.

The functional groups and types of bonds of materials were determined using FTIR. As presented in Fig. 5a, the narrow peak within the 3400–3650 $cm^{-1}$ range is a characteristic of –OH stretching vibration [2,3]. After MgO modification, the peaks at 1032 and 1648 $cm^{-1}$, corresponding to C-O-Mg and C═O stretching vibrations, were observed [52,53]. The C—N stretching vibration at 1184 $cm^{-1}$ could be due to the intrinsic nitrogeneous components, and the bond disappearing due to MgO enhancement and surface chemistry alteration, or formation of other nitrogen and/or oxygen-containing functional groups [54,55]. The 2895 $cm^{-1}$ and 742 $cm^{-1}$ peaks are attributed to asymmetrical and symmetrical stretching vibrations of C—H bonds in aliphatic hydrocarbons [56,57]. The aromatic ring structure at 1570 $cm^{-1}$, corresponding to C═C stretching vibration, shifted to 1522 $cm^{-1}$ after MgO modification and thermal activation [58,59]. The MgO treatment increased oxygen-containing functional groups that enhanced the removal of $NH_4^+$ from feed water.

The crystallinity of the material was determined using X-ray diffraction (XRD). Fig. 5b illustrates narrow peaks at 21.69° and 44.45°, corresponding to the graphitic (002 and 100) planes [26,60]. The diffraction plane (200) observed in OP-400@0.5, OP-400@1.0, and OP-400@1.5 may be attributed to cubic MgO structures and the brucite structure ($Mg(OH)_2$) diffraction plane (102), as similarly observed by Lv et al. [61].

The MgO modification enhanced the $NH_4^+$ removal by improving the ion-exchange capacity of MgO and $Mg(OH)_2$, hence facilitating $NH_4^+$ adsorption through electrostatic attraction and ion exchange mechanisms.

The pore size distribution and the specific surface area of carbon material significantly affect the adsorption capacity. Fig. 5c illustrates the nitrogen gas adsorption/desorption isotherm type I for OP-400 and type IV for OP-400@0.5, OP-400@1.0, and OP-400@1.5 based on the International Union of Pure and Applied Chemistry (IUPAC) classification. The hysteresis loop in the MgO-modified sample indicated the development of mesopores that favored the $N_2$ adsorption-desorption at relative pressure above 0.4 [62]. As observed in Fig. 5d, the NLDFT

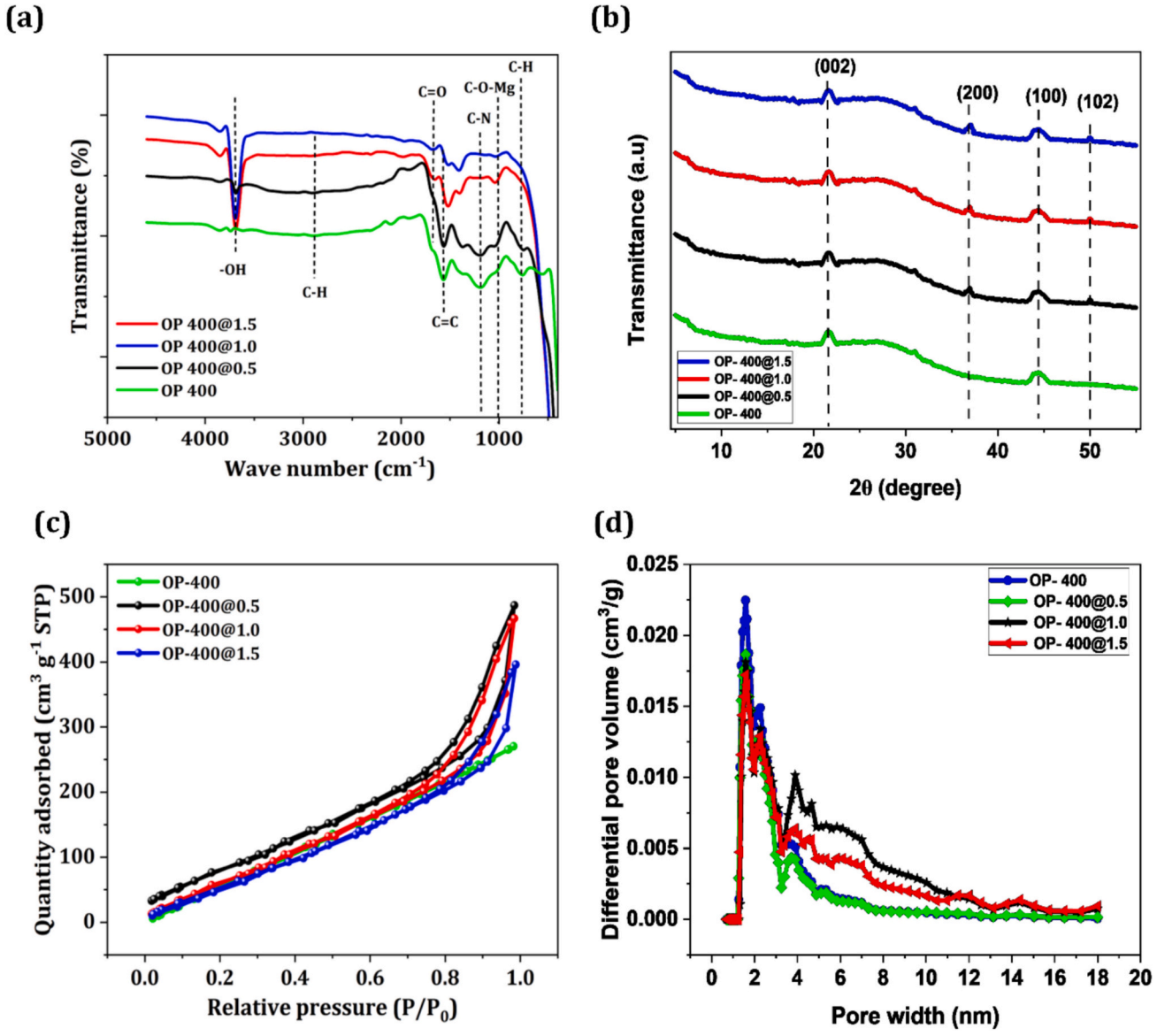


**Fig. 5.** Shows (a) FTIR spectra, (b) XRD patterns, (c) $N_2$ adsorption–desorption isotherms, and (d) pore size distribution of OP-400, OP-400@0.5, OP-400@1.0, and OP-400@1.5 electrode materials.

revealed the pore size distribution profile. OP-400 displayed a high specific surface area primarily due to its micropores. The observed decrease in specific surface area for OP-400@0.5, OP-400@1.0, and OP-400@1.5 may be attributed to the MgO modification, which introduced mesopores, as illustrated in Table 1. This finding is consistent with the report by Li et al. [2,3]. The average pore size in OP-400 was observed to be 1.82 nm, and after MgO modification, the pore sizes increased to 1.86, 4.38, and 4.53 nm for OP-400@0.5, OP-400@1.0, and OP-400@1.5, respectively. The introduced mesopores enhanced diffusion and adsorption kinetics, while micropores facilitated $NH_4^+$ adsorption capacity from feed water.

The observed trend of increasing average pore sizes and decreasing specific surface area in biochar, as detailed in Table 1, resulted in a corresponding decline in $NH_4^+$ adsorption capacity. Micropores are recognized for their significance in adsorbing small molecules like $NH_4^+$, while larger pores can facilitate diffusion rates while potentially compromising overall adsorption capacity, as discussed in previous studies by Kumar et al. [63]. The pore volume exhibited a notable rise from the pristine (0.362 $cm^3\ g^{-1}$) biochar to 0.722 $cm^3\ g^{-1}$ for OP-400@1.5. This increase in pore volume corresponded with the higher MgO ratio, indicating enhanced pore development resulting from the activation process. Larger pores present in OP-400@1.0 and OP-400@1.5 accelerated the diffusion rate of $NH_4^+$ to adsorption sites, reducing overall RE. Conversely, the enriched micropores and relatively high specific surface area of OP-400@0.5 contributed to its superior adsorption capacity. Despite the high specific surface area of OP-400, it lacked essential surface functionalities. The distinctive characteristics of OP-400@0.5, characterized by an optimal combination of micropores and specific surface area, position it as a suitable candidate for $NH_4^+$ removal applications due to its enhanced adsorption capacity and effective surface interactions.

The degree of disorder in OP-400 and OP-400@0.5 was assessed by Raman spectroscopy to evaluate the effects of MgO modifications. Spectral lines of OP-400 and OP-400@0.5 exhibited two significant peaks at 1580 $cm^{-1}$ and 1350 $cm^{-1}$, corresponding to the G-band and the D-band, respectively. As demonstrated in Fig. 6a, the OP-400 sample was observed with high graphitic ordering compared to OP-400@0.5, reflecting the amorphous characteristics of the carbon [64]. The $I_D/I_G$ ratios of OP-400 (0.726) and OP-400@0.5 (0.859) indicated that MgO modification enhanced the OP-400@0.5 sample to be more porous and disordered. This disorder contributed to greater pore sizes and more active sites for adsorption. The TGA analysis was divided into two distinct steps, namely Step I and Step II. Step I, as illustrated in Fig. 6b, targeted the removal of loosely bound water, while Step II corresponded to the pyrolytic phase. Notably, all materials exhibited comparable weight loss, with equivalent onset temperatures (350 °C) and final degradation temperatures (500 °C). As a result, these materials exhibit thermal stability up to 500 °C. Since the biochar's porosity is determined by its surface area and the presence of micropores and mesopores that can hold onto loosely bound water, this was evident in Step I. This step showed the level of surface hydrophilicity and pore accessibility. In Step II, the biochar materials remained stable up to 500 °C, indicating their ability to maintain porosity and surface chemistry during operations. This preservation helps retain adsorption and electrochemical properties, enabling the biochar to withstand multiple redox cycles without losing capacitance and conductivity [65,66]. Therefore, the combination of porosity and hydrophilicity supports the efficiency of ion removal, improving removal rates and electrode durability.

The impact of MgO modifications was observed through a notable change in the elemental composition, as determined by XPS (Table 2), where a decrease in C and O contents was noted. Carbon content decreased from 79.01 to 69.86 %, possibly due to partial oxidation and removal of aliphatic carbon structures. A decrease in oxygen content from 2.83 % to 2.27 % was observed, attributed to the introduction of oxygen-containing functional groups. The possibility exists that some oxygen functionalities may decompose at higher temperatures, as supported by Kharel et al. [67] and Nzediegwu et al. [68]. A slight increase in N content, from 18.16 to 25.40 %, could be due to nitrogen enrichment during activation in the tube furnace.

Additionally, the activation of MgO has the potential to create defects that stabilize nitrogen-containing functional groups initially present in biomass, as observed by Schievano et al. [66]. Modification of MgO was successfully observed for OP-400@0.5 biochar with 2.47 % content. The decrease in elemental composition levels, coupled with a slight rise in nitrogen (N) content, resulted from the impact of MgO

**Table 2**
Elemental composition of orange peel-derived biochar.

| Sample/elemental (%) | C | O | N | Mg |
|---|---|---|---|---|
| OP-400 | 79.01 | 2.83 | 18.16 | 0.00 |
| OP-400@0.5 | 69.86 | 2.27 | 25.40 | 2.47 |

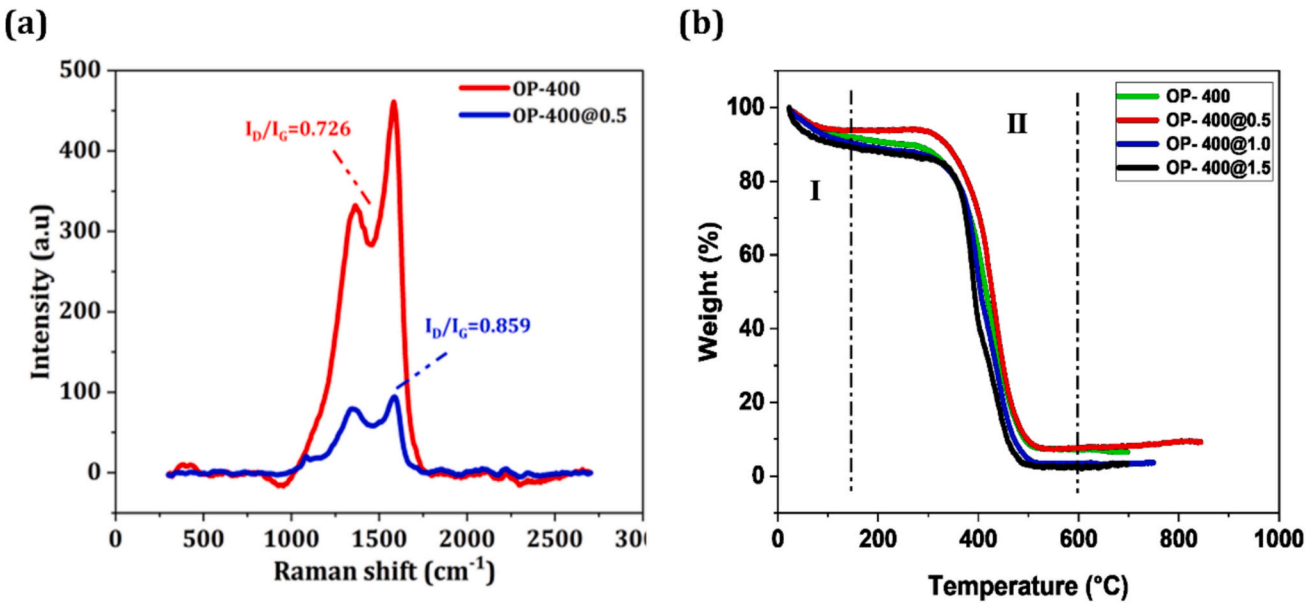


**Fig. 6.** Shows (a) Raman shifts for OP-400 and OP-400@0.5 (b) TGA profiles for OP-400 and OP-400@0.5, OP-400@1.0, and OP-400@1.5 electrode materials.

modifications. This effective integration of MgO into the OP-400@0.5 biochar surface enhances its ion exchange capacity and electrosorption capacity, consequently improving the overall RE and AARR.

Elemental composition of OP samples and chemical bonds of C, O, N and Mg were analyzed by XPS (Fig.7). Full spectra (Fig. 7a), an analytical comparison between unmodified OP-400 and modified OP-400@0.5 reveals significant peaks for C1s (~285 eV) and O1s (~532 eV), indicating the presence of carbon and oxygen as primary elements in both samples. Notably, the OP-400@0.5 sample shows additional peaks not found in OP-400, including Mg1s (~1304 eV), Mg2p (~48 eV), Mg2s (~ 85 eV), and Mg KLL Auger peaks, confirming the successful integration of magnesium species post MgO modification. A minor N1s peak is also detected in both biochar samples, indicating nitrogen enrichment introduced during modification or originating from the precursor material. The intensified O1s peak in OP-400@0.5 suggests an increase in oxygen-containing functional groups, likely stemming from MgO and potential $Mg(OH)_2$ formation. According to Fig. 7b, the Mg1s spectrum for OP-400@0.5 showcases metallic Mg, C-MgO, and $Mg(OH)_2$, peaks, confirming MgO as the primary magnesium species post-modification.

The carbon bonds in the biochar materials were subsequently showcased in Fig. 7c and d. The C1s spectrum, as shown in OP-400, showcased components typical of biochar, including C—H (~284.5 eV), C—C (~284.3 eV), C—O (~285.7 eV), and C-O-C (~288.8 eV) groups. In contrast, OP-400@0.5 displayed peaks for C—H (~284.6 eV), C—O (~285.6 eV), and a new C═O (~286.6 eV) component. OP-400@0.5 exhibits increased oxygenated carbon species that improve electrosorption. Fig. 7e and f demonstrates the oxygen bonds observed in the XPS O1s spectrum. OP-400 biochar shows oxygen mainly as C—O (~533.5 eV), C═O (~531.1 eV), and O-C=O (~532 eV). Additional peaks in the O1s spectrum for OP-400@0.5 suggest enhanced electrostatic interactions and redox activity. The N1s spectrum (Fig. 7g and h), for OP-400@0.5, shows graphitic and pyridinic nitrogen that facilitate charge transfer, improve electrical conductivity, and stabilize the porous structure. It also enhances minor pseudocapacitance attributed to pyridinic nitrogen, an impact of the modification [27,69]. Therefore, OP-400@0.5 showcases significant enhancements in surface functionalities. These include increased oxygenated carbon species, stronger electrostatic interactions facilitated by more surface oxygen groups and MgO, and improved electrochemical activity through the presence of graphitic and pyridinic nitrogen species. These improvements demonstrate superior performance of high RE and AEC in electrosorption compared to OP-400. Notably, the spectral data highlight the enhanced ion exchangeability and electrosorption of OP-400@0.5, particularly beneficial for FCDI.

### 3.2. Electrochemical performance

An electrochemical test is crucial for evaluating the electrosorption performance of the material. The CV analysis was carried out on the OP-400 and OP-400@0.5 electrodes, with varying scan rates (CV) (Fig. 8a and b). The CV profile of both OP-400 and OP-400@0.5 electrodes suggests an electric double-layer capacitance (EDLC) transport mechanism. In comparison, OP-400 exhibited a smaller and significantly distorted rectangular CV curve, suggesting a lower charge storage capacity than that of OP-400@0.5 electrode. The lack of redox peaks during both anodic and cathodic sweeps is evident, indicating that MgO is electrochemically inactive, which aligns with the findings of Karthikeyan et al. [44]. The enhanced capacitance in OP-400@0.5 at slow scan rates could be attributed to accessible micropores, optimal pore size distribution, or the presence of pseudocapacitive effects due to surface functional groups (Fig. 5a). These attributes can lead to greater charge storage per unit area than observed in conventional EDLC materials [24,70,71]. Therefore, MgO plays a crucial role in maintaining the structural integrity of the OP-400@0.5 electrode, ensuring its stability during extended cycling. Numerous micropores contribute to a high specific surface area, but this may not always be the case as very narrow micropores can hinder ion transfer, decreasing the effective surface area for ion adsorption. Therefore, a high specific surface area in electrodes does not always guarantee enhanced specific capacitance [72–74]. The OP-400@0.5 exhibit high specific capacitance at low scan rates. The CV curves of OP-400@O.5 showed a nearly perfect rectangular shape at low scan rates, maintaining this shape even at higher scan rates with slight distortion. This indicates a rapid and unhindered charge transfer process facilitated by the *meso-*/micropore combination. The Nyquist profile for OP-400 and OP-400@0.5 is illustrated in Fig. 8c. A low ohmic resistance (Rs) improves interfacial contact efficiency, facilitating current flow and energy storage while minimizing losses at the electrode-electrolyte interface [75,76]. The Rs for OP-400 and OP-400@0.5 materials were 2.42 Ω and 0.06 Ω, respectively. In comparison, the charge transfer resistance (Rct) of OP-400@0.5 at high frequency was observed with a small circle (3.67 Ω) compared to that of OP-400 (5.41 Ω), indicating a low polarization effect. The same observation was reported by Sufiani et al. [77]. Also, OP-400 was observed to have high ion diffusion resistance at low frequency as compared to OP-400@0.5, this observation align with bode plots results (Fig. 8e). Therefore, Low Rs, Rct, and ion diffusion resistance for OP-400@0.5 can be due to better pore structure and enhanced cavity formation that enhances ion diffusion rate [2,3]. The specific capacitance from CV calculated using Eq. (1) was 125 F $g^{-1}$ for OP-400 and 238 F $g^{-1}$ for OP-400@0.5 at a scan rate of 1 mV/s (Fig. 8d).

The enhanced characteristics of OP-400@0.5 were further revealed through Bode plots (Fig. 8e), which showed minimal absolute impedance at both high and low frequencies compared to the OP-400 electrode. The phase angle analysis indicated a high characteristic frequency at $-45^{\circ}$ for OP-400@0.5, reflecting a lower time constant of 0.85 ms compared to 0.94 ms for OP-400 using Eq. (3). [78,79]. The GCD tests for the OP-400 and OP-400@0.5 electrodes (Fig. 8f and g) involved varying current densities from 5 to 1 A $g^{-1}$, where Eq. (2) was used to calculate the specific capacitance within the employed potential window of −1.0-0.0 V. The symmetrical and linear features of the charge-discharge profiles served as additional evidence for the EDL behavior of the electrodes (Fig. 8f and g). The specific capacitance (Fig. 8h) exhibits that the MgO-modified electrode (OP-400@0.5) provided the highest specific capacitance of 194 F $g^{-1}$ compared to 77.43 F $g^{-1}$ of the unmodified electrode (OP-400). The cyclic stability of OP-400@0.5 electrode is a crucial factor to be considered, where a long-term charge-discharge performance was conducted at 2 A $g^{-1}$ (Fig. 8i). The GCD profiles for the initial and 5000th cycles (Fig. 8i, inset) demonstrate a consistent capacitive retention (CR) of 94.11 % and coulombic efficiency (CE) of 93.54 %. Moreover, the electrode displays excellent CR and CE over 5000 cycles, affirming its stability and reliability for extended use. The enhancement in energy storage capacity resulting from reduced impedance, structural stabilization that led to increased charging and discharging durations, supported by the lower time constant of 0.85 ms [75,80]. The improved characteristics of OP-400@0.5 are evident in reduced impedance, higher capacitance values, and lower time constants, indicating its potential for enhanced performance in energy storage and providing valuable insights in FCDI applications.

### 3.3. Wettability measurements

The wettability characteristics of the modified and unmodified biochar materials were analyzed, as depicted in Fig. 9. The initial contact angles for OP-400 and OP-400@0.5 were recorded at 101.5° and 67.1°, respectively. Over time, the contact angle for OP-400 decreased to 67.1 degrees within 40 s, while for OP-400@0.5, it vanished entirely after 12 s. This shows that OP-400@0.5 is more hydrophilic than OP-400. Hydrophilic biochar improves electrosorption in FCDI by enhancing water interaction and ion accessibility. The presence of oxygenated functional groups, such as C—O, C═O, and -OH, as observed in FTIR (Fig. 5a), enhances wettability, allowing electrolytes to penetrate pores effectively

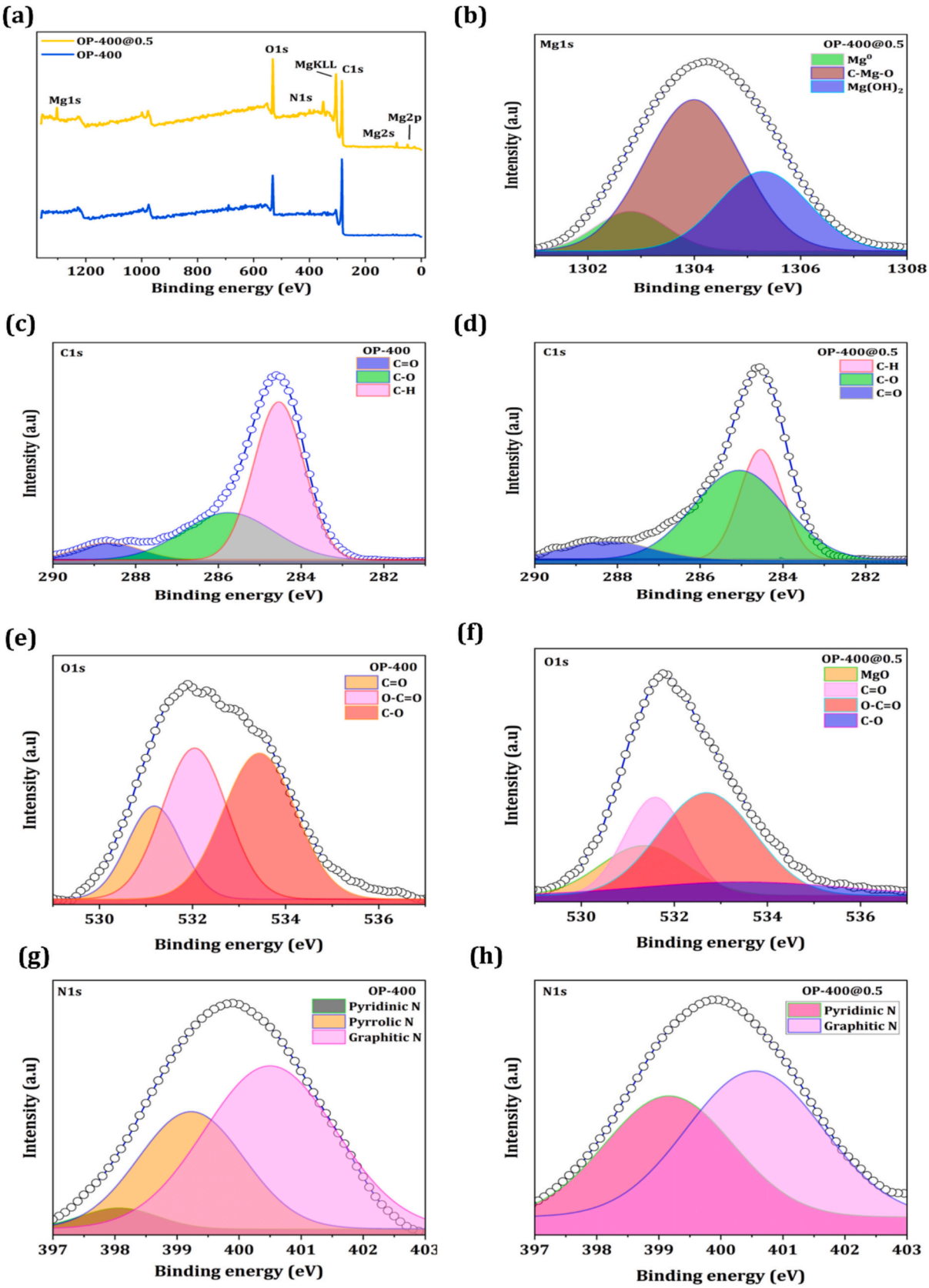


**Fig. 7.** XPS spectra of OP-400 and OP-400@0.5 (a) full spectra, (b) Mg1s of OP-400@0.5, (c–d) C1s, (e–f) O1s, (g–h) N1s.

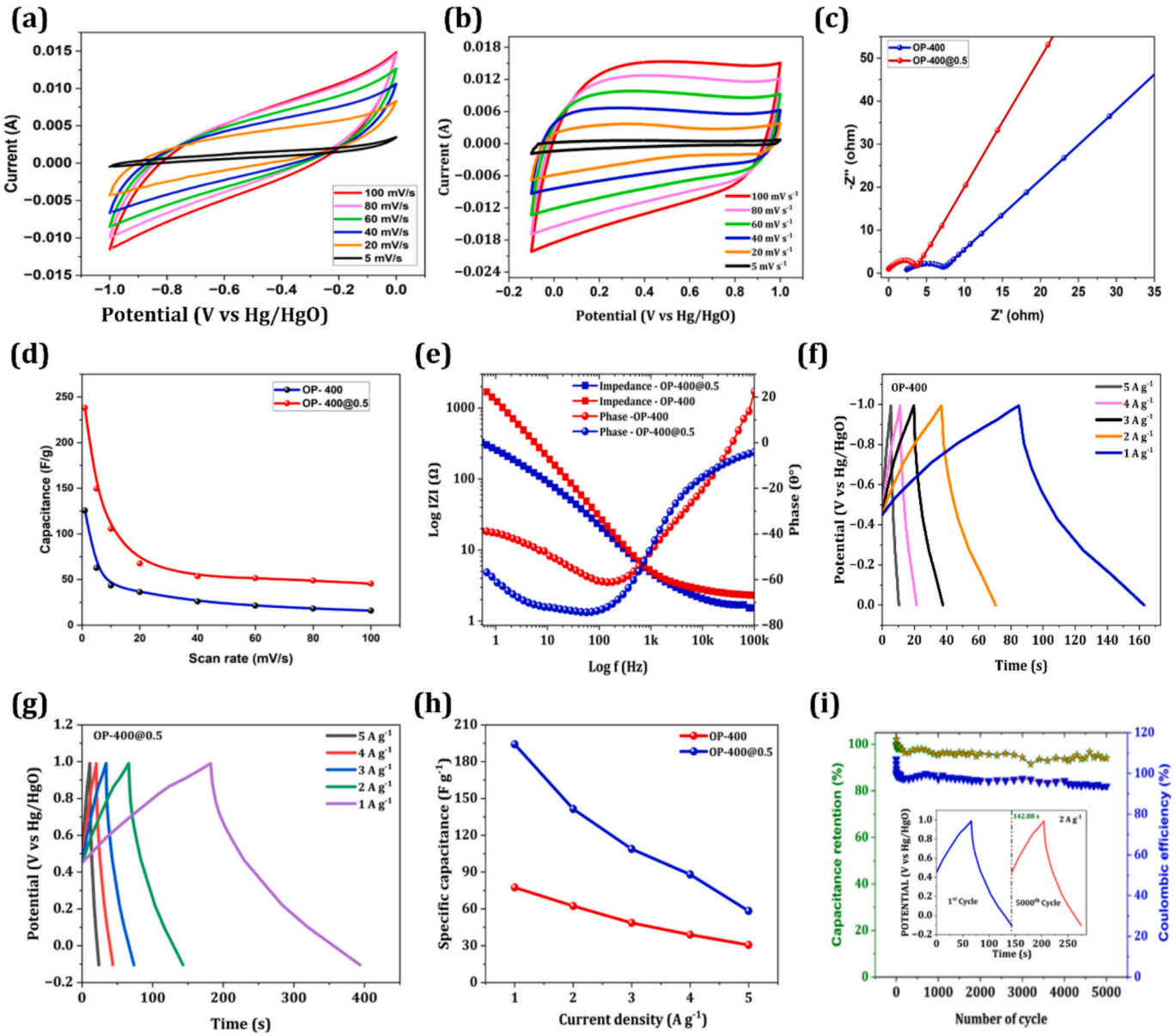


**Fig. 8.** Shows CV of (a) OP-400, (b) OP-400@0.5 at different scan rates, (c) Nyquist profiles, (d) CV specific Capacitance, (e) Bode plots for OP-400 and OP-400@0.5 electrodes, (f) GCD for OP-400, (g) GCD for OP-400@0.5, (h) GCD specific capacitance of OP-400 and OP-400@0.5 electrodes, (i) CR and CE efficiency of OP-400@0.5 electrode at 2 A $g^{-1}$ current density.

and increase ion adsorption capacity [81]. Hydrophilic surfaces also reduce electrical resistance, optimizing charge transfer during electrosorption. Tailored functional groups, such as hydroxyl, in modified hydrophilic biochar, elevate selectivity and enhance adsorption for specific ions [82]. The OP-400 biochar, with aliphatic functional groups and fewer aromatic bonds, exhibited lower hydrophilicity in comparison to the modified OP-400@0.5 biochar. The MgO modification of OP-400@0.5 biochar resulted in the formation of oxygenated carbon bonds, as confirmed by XPS and FTIR analyses, along with an increase in pore size, as shown in Table 1; this observation was also reported by Alfredy et al. [8]. The increased pore sizes of OP-400@0.5 enhanced the surface area available for water interaction, thereby improving moisture retention, which is necessary for FCDI electrodes.

### 3.4. Removal of $NH_4^+$ by FCDI system under different operational conditions

#### 3.4.1. FCDI performance of different flow electrodes

The research optimized the performance of prepared biochar samples to determine the most suitable for maximum $NH_4^+$ electrosorption. Experiments were performed under an applied voltage of 1.2 V, a pH of 6, a carbon content of 2.5 wt%, a flow rate of 10 mL min-1, a charging time of 120 min, and a pH of 6. A 500 mg $L^{-1}$ of $NH_4^+$ was prepared as the initial concentration of the feed solution. As illustrated in Fig. S6, the initial pH of 6 was modified using 0.1 M HCl or 0.1 M NaOH before the experimental trial. The final pH values recorded were 8.1, 8.0, and 7.8 for the OP-400, OP-400@1.0, and OP-400@1.5 electrodes, respectively. In contrast, the OP-400@0.5 electrode concluded with a final pH value of 6.2. Fig. 10a shows that the RE results (Eq. (4)) for the samples revealed varying performance levels. The OP-400 biochar achieved a RE value of 51.5 %, while OP-400@0.5 exhibited a significantly higher RE

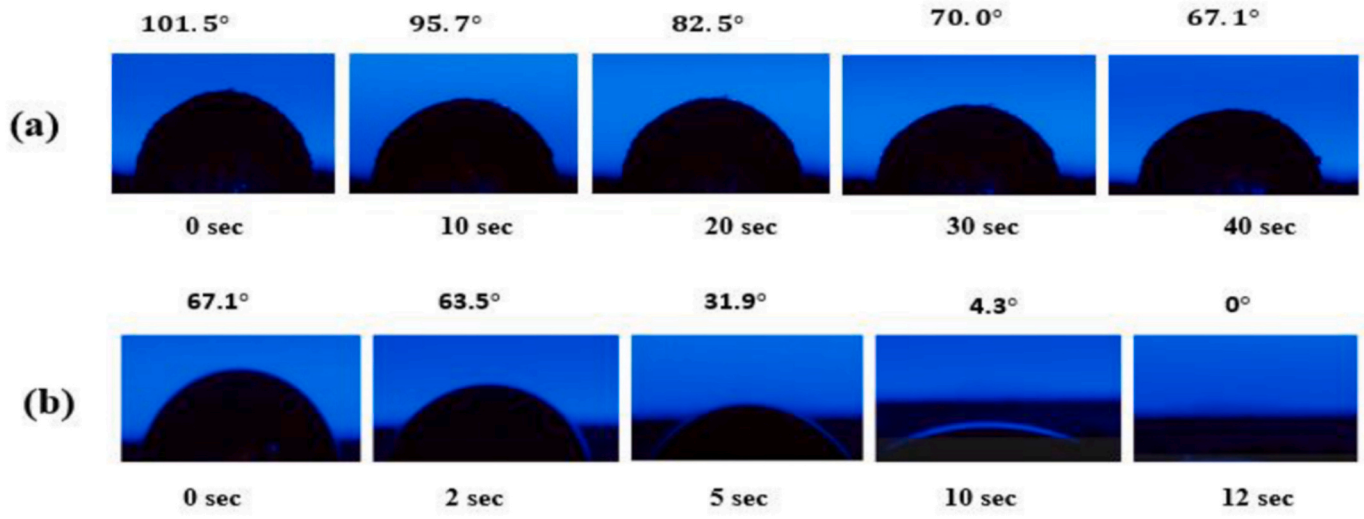


**Fig. 9.** Shows the wettability properties of (a) OP-400 and (b) OP-400@0.5 electrodes.

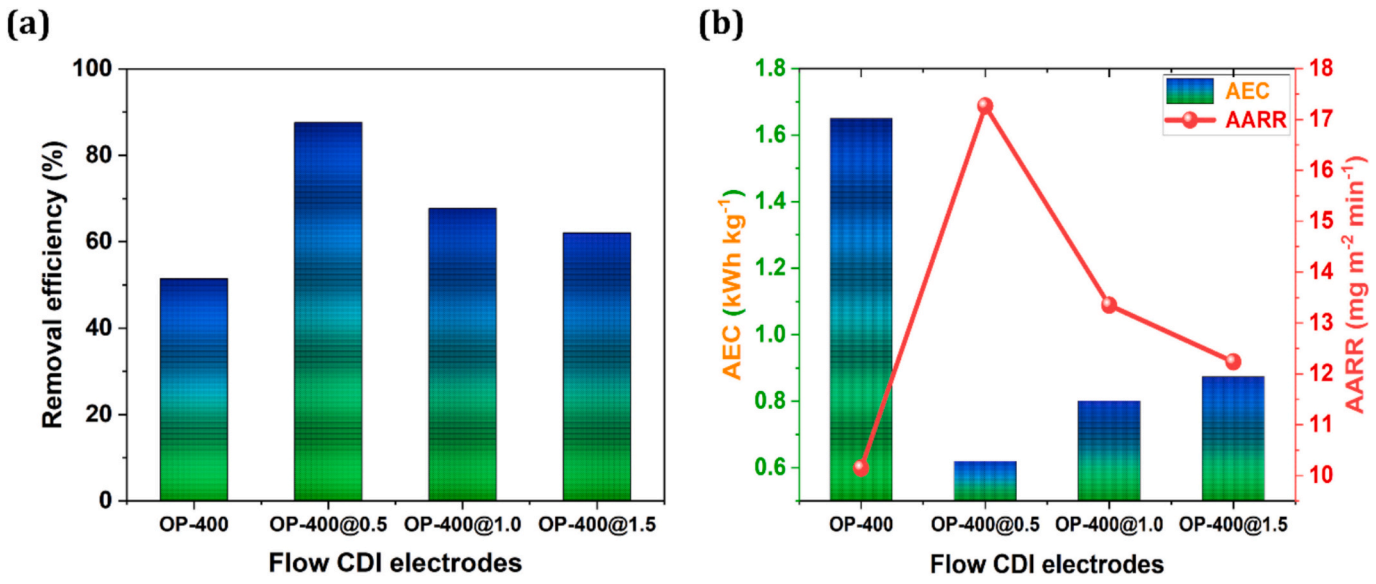


**Fig. 10.** Shows (a) RE, (b) AEC, and AARR of OP-400, OP-400@0.5, OP-400@1.0, and OP-400@1.5 electrode materials. The experiment was conducted at pH 6, with a 2.5 wt% carbon content, an applied voltage of 1.2 V, and a feed solution of 500 mg $L^{-1}$, under a charging time of 120 min.

of 87.6 %. OP-400@1.0 and OP-400@1.5 showed intermediate RE values of 67.7 and 62 %, respectively. Fig. 10b indicates that the AEC and AARR values of the samples varied significantly when using Eqs. (7) and (8). OP-400 exhibited the highest AEC at 1.65 kWh $kg^{-1}$.

In comparison, OP-400@0.5 demonstrated a substantial reduction in AEC with a value of 0.62 kWh $kg^{-1}$. OP-400@1.0 and OP-400@1.5 showed intermediate AEC values of 0.8 and 0.87 kWh $kg^{-1}$, respectively. The exceptional electrosorption efficiency of OP-400@0.5 is linked to its reduced $R_s$ and $R_{ct}$ impedances, elevated specific capacitance, and hydrophilic properties. This particular sample exhibits a significant abundance of oxygenated carbon bonds, alongside graphitic and pyridinic nitrogen, which facilitates a higher number of active sites for improved electrosorption. These characteristics collectively enhance the superior performance of OP-400@0.5 when compared to other biochar variants in the FCDI system.

### 3.4.2. FCDI performance at different flow rates

Identifying an optimal flow rate is crucial for enhancing FCDI system performance. The impact of varying electrode flow rates (5, 7.5, 10, and 12.5 mL $min^{-1}$) on FCDI operations using a 1.2 V applied voltage and 2.5 wt% carbon content was investigated. Fig. 11 shows the results, indicating that at flow rates of 5 and 7.5 mL $min^{-1}$, the RE increased from 54.7 % to 68.9 %. Upon further increasing the flow rate to 10 mL $min^{-1}$, RE improved to 86.5 %, but then decreased to 69.5 % at 12.5 mL $min^{-1}$. When the flow rate exceeds 10 mL $min^{-1}$, the RE gradually decreases. This reduction could be due to the shorter residence time of the electrode in the FCDI system at higher flow rates, which diminishes the contact duration between the feed solution and the electrode. Higher flow rates promote ion migration transport under an electric field but diminish capacitive double-layer storage, whereas lower rates are conducive to capacitive trapping [83]. This suggests that the optimal condition for subsequent experiments was identified at a flow rate of 10 mL $min^{-1}$.

### 3.4.3. FCDI performance on different applied voltages

This study examined how applied voltage affects the FCDI system, while maintaining other operating conditions at a 10 mL $min^{-1}$ flow rate, pH 6, and 2.5 wt% carbon content. Fig. 12 shows the RE against

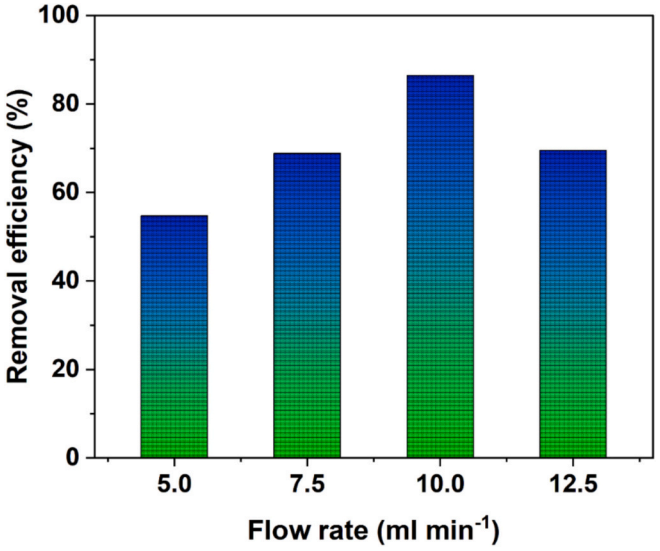


**Fig. 11.** Shows the RE against flow rate variations of OP-400@0.5, under 1.2 V applied voltage, 2.5 wt% carbon content as operating conditions, subject to 500 mg $L^{-1}$ initial concentration of feed solution.

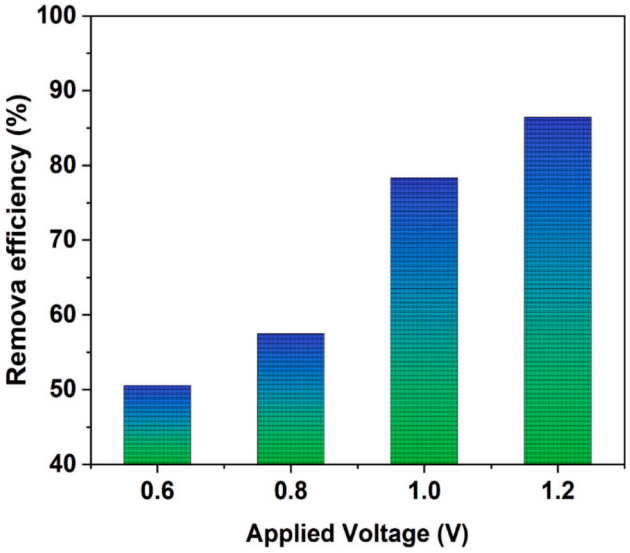


**Fig. 12.** RE against applied voltage changes of OP-400@0.5, under 10 mL $min^{-1}$ flow rate, 2.5 wt% carbon content as operating conditions, subject to 500 mg L-1 initial concentration of feed solution.

applied voltages from 0.6 to 1.2 V. The removal rates were determined to be 50.6 %, 57.5 %, 78.3 %, and 86.5 % at 0.6, 0.8, 1.0, and 1.2 V, respectively. The RE was observed to increase as the applied voltage increased. The increase in applied voltage in the FCDI system enhances the formation of the electrical double layer [2,3,84], resulting in improved charge storage and enhanced ion movement. Increasing the applied voltage results in a boost in electric field strength, enhanced charge transfer efficiency, and reduced concentration polarization [13,85]. The findings indicate that the RE rises with higher applied voltages; however, to prevent faradaic reactions, 1.2 V was determined as the optimal voltage for the subsequent experiments.

### 3.4.4. FCDI performance on different initial pH

The influence of pH levels on $NH_4^+$ removal in water is a critical factor to consider. This research investigated the impact of pH variations ranging from 5 to 8, which is the typical pH range for most water samples. The experiment was performed at an applied voltage of 1.2 V, a carbon content of 2.5 wt%, and a flow rate of 10 mL $min^{-1}$ as the operating conditions. The experimental observations revealed minor fluctuations in both initial and final pH values. Notably, the transitions observed were from pH 5 to pH 7, pH 6 to pH 6.7, pH 7 to pH 7.7, and pH 8 to pH 8.1 (refer to Fig. S7 from Supporting information). Prior to the experimental trials, the initial pH of 6 was meticulously adjusted using either 0.1 M HCl or 0.1 M NaOH. Fig. 13 presents the study results, illustrating the corresponding RE relative to the initial pH levels. Notably, at pH 5, the RE was measured at 75.6 %, showcasing a noticeable increase to 86.7 % at pH 6. However, with a further rise in pH to 7 and 8, the RE declined significantly to 82 % and 67.7 %, respectively. At low pH (pKa < 9.2), $NH_4^+$ predominates, facilitating efficient removal through electrosorption due to its charged nature with reduced energy consumption. Conversely, at higher pH levels (pKa > 9.2), selective trapping of $NH_3$ in flow electrodes enhances ammonia adsorption, yielding valuable ammonia-rich solutions [86,87]. Therefore, controlling pH levels strategically can optimize the highest removal efficiency of $NH_4^+$ at lower pH. Consequently, pH 6 emerged as the optimal condition for consistent $NH_4^+$ removal across all experimental trials.

### 3.4.5. FCDI performance under different carbon content

In this study, the effect of carbon content was investigated. The impact of increasing carbon content on the RE during FCDI operation can be observed in Fig. 14. Carbon contents of 1.0, 1.5, 2.0, and 2.5 wt% were employed under the following operational conditions: 1.2 V applied voltage, initial pH 6, flow rate of 10 mL $min^{-1}$, and duration of 120 min. The results displayed a notable and gradual rise in RE, ranging from 54 to 86.5 %, corresponding to carbon contents of 1.0 to 2.5 wt%, respectively. The observed improvement could be attributed to the increased surface area, active sites, reduced charge loss, and reduced internal resistance. Elevating the carbon content in the flow electrode demonstrates improved desalination efficiency, increased capacitance, reduced energy consumption, and sustained flow properties [88,89]. The heightened carbon content facilitates improved charge transfer, augmenting the active material available for ion adsorption. Moreover, conductivity within the flow electrode slurry is enhanced, leading to minimized charge loss during operation and reduced internal resistance [2,3,90]. This advancement accelerates ion electrosorption due to the increased surface area and improved electrical connectivity, thereby enhancing removal kinetics during operation. Following the

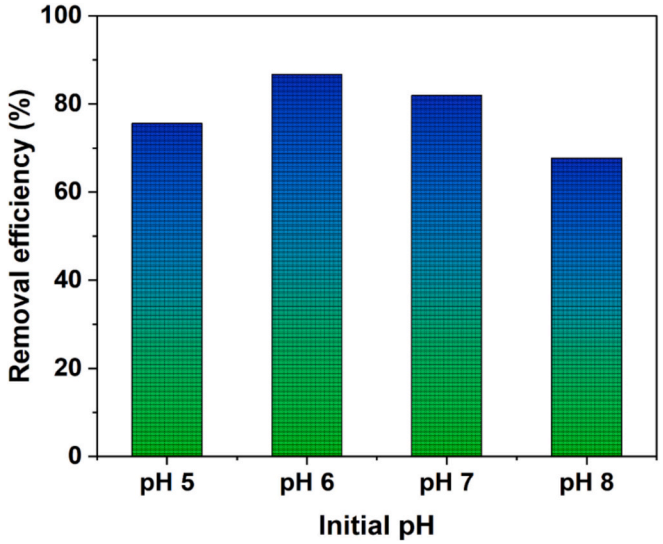


**Fig. 13.** RE against initial pH dynamics of OP-400@0.5, under 1.2 V applied voltage, 2.5 wt% carbon content as operating conditions, subject to 500 mg $L^{-1}$ initial concentration of feed solution.

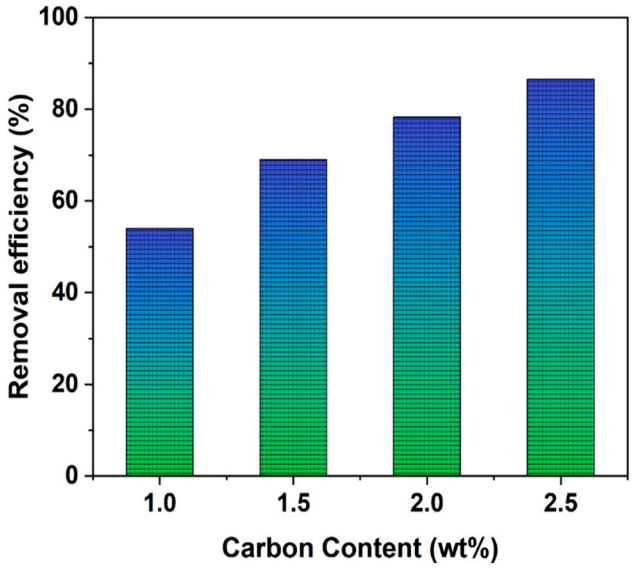


**Fig. 14.** RE against carbon content (wt%) of OP-400@0.5, under 1.2 V applied voltage, initial pH 6, as operating conditions, subject to 500 mg $L^{-1}$ initial concentration of feed solution.

experimental design (14.4 $cm^2$ FCDI cell), the optimal carbon content of 2.5 wt% was suggested for subsequent experiments. Beyond this threshold, an increase in active material content resulted in elevated pressure within the tubes, leading to clogging and system disruption.

### 3.4.6. FCDI performance for continuous cycles

During the $NH_4^+$ removal and cycling processes, it was observed that $NH_4^+$ ions were effectively desorbed from the OP-400@0.5 electrode, achieving an impressive desorption efficiency (DE) of 84.4 %. This efficiency was successfully retained over 30 complete cycles using the same electrode. Subsequent cycle tests (Fig. 15a) showed that the DE remained stable at 90.6 %, 90.4 %, and 84.4 % during the 10th, 20th, and 30th cycles, respectively. The stability could be attributed by MgO modification that claim to stabilize carbon matrix structure [44]. The slight decrease in efficiency may be attributed to factors such as electrode degradation, ion accumulation, pore blockage, or oxidative damage [91,92]. Notably, remarkable desorption efficiency (Fig. 15b) was maintained across all 30 cycles, likely due to the strategic use of voltage polarity reversal (−1.2 V) for 120 min. and the presence of a functionalized electrode surface, structural stability, facilitated ion exchange, and electrosorption [93,94]. After each experimental trial, the OP-400@0.5 electrode was treated with 0.1 M HCl, stirred for 5 min, and then washed with deionized water until the conductivity dropped below 10 μS $cm^{-1}$.

### 3.4.7. FCDI performance in co-existing ions

In examining the performance of electrosorption and the selectivity of the FCDI system utilizing OP-400@0.5 as the flow electrode for $NH_4^+$ in actual wastewater, we simulated standard municipal wastewater containing the common co-existing cations $Na^+$ and $Ca^{2+}$. The experimental trials were designed as single, multiple 1, multiple 2, and multiple 3 as adopted from Li et al. [2,3]. The simulated municipal wastewater was prepared by dissolving 3.78 mM $NH_4^+$ in all trials. In the single trial, only $NH_4^+$ was involved; in multiple 1, 3.78 mM $NH_4^+$ and 1.89 mM $Na^+$ were used; for multiple 2, 3.78 mM $NH_4^+$ and 1.89 mM $Ca^{2+}$ were employed; and in multiple 3, 3.78 mM $NH_4^+$, 0.945 mM $Na^+$, and 0.945 mM $Ca^{2+}$ were included. Fig. 16 illustrates a decline in $NH_4^+$ removal efficiency from 87.6 to 78.2, 71.6, and 68.9 % with increasing levels of $Na^+$ and $Ca^{2+}$. Despite the elevated concentrations of interfering ions, the FCDI system consistently removed $NH_4^+$, demonstrating the selectivity and resilience of the OP-400@0.5 flow electrode. The selectivity of OP-400@0.5 for $NH_4^+$ compared to $Na^+$ and $Ca^{2+}$, as calculated using Eq. (2), was significantly greater than 1 ($Na^+$: 3.08; $Ca^{2+}$: 2.02; $Na^+/Ca^{2+}$: 1.59), reinforcing these findings. Additional details for these findings are provided by GCD and CV plots (see Fig. S5 from the Supporting information). The OP-400@0.5 electrode in $(NH_4)_2SO_4$ demonstrates enhanced capacitance values compared to NaCl and $CaCl_2$ electrolytes, indicating an enhanced charge storage capacity. The absence of faradaic reactions in $(NH_4)_2SO_4$ leads to EDL behavior, while less EDL behavior in the transport mechanism in NaCl and flattened EDL in $CaCl_2$. The high specific capacitance results and GCD tests highlight the superior performance of the OP-400@0.5 electrode in $NH_4^+$ compared to $Na^+$ and $Ca^{2+}$ electrolytes (details in Supporting

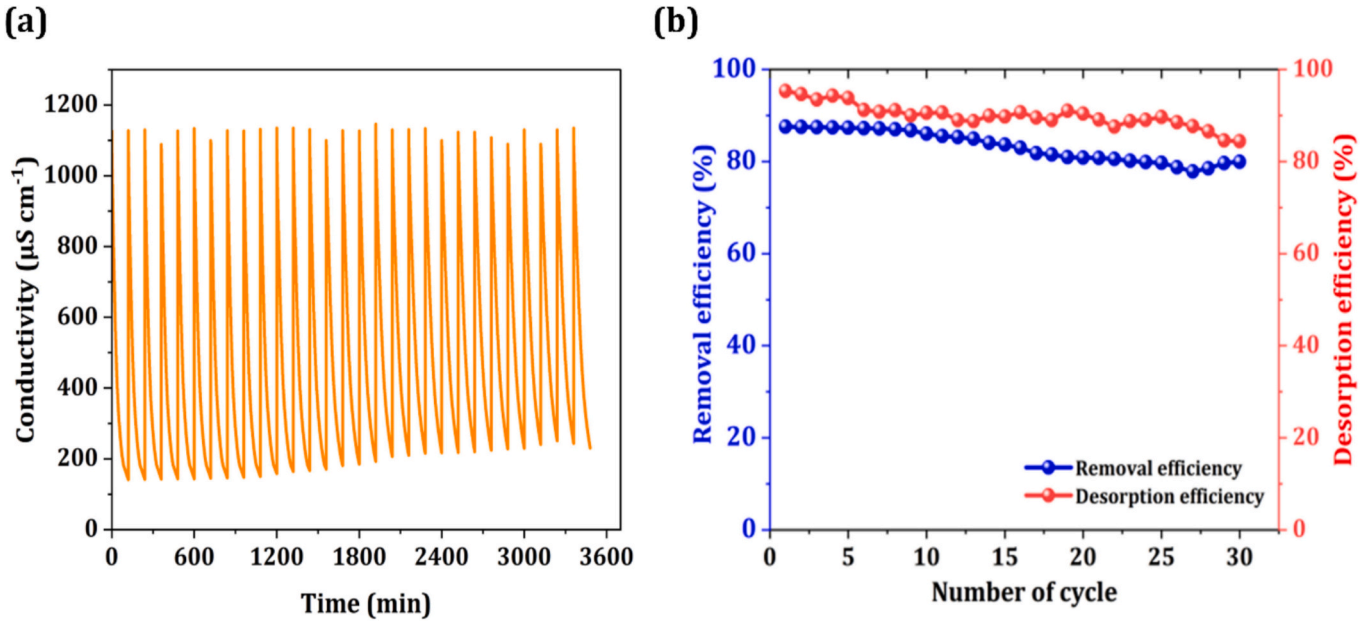


**Fig. 15.** Reusability experiment (a) conductivity trends, (b) removal and desorption efficiency of OP-400@0.5 electrode at electrosorption voltage of 1.2 V, using feed solution of 500 mg $L^{-1}$ at 10 mL $min^{-1}$.

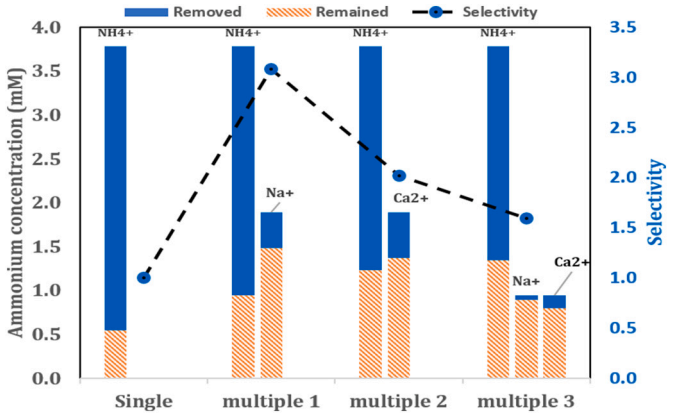


**Fig. 16.** Removed and Remaining ion concentration of $NH_4^+$, $Na^+$, and $Ca^{2+}$ and respective selectivity.

information). The MgO-biochar composite substantially enhances the selectivity of $NH_4^+$ by integrating the distinct properties of each constituent. The sustainable, porous structure of biochar increases adsorption capacity and supports nutrient retention, while also providing mechanical stability conducive to long-term ion exchange efficiency [95,96]. Conversely, MgO contributes by establishing an alkaline environment that promotes $NH_4^+$ ion adsorption, alongside introducing structural defects that function as electron reservoirs, thereby facilitating chemical activity. Collectively, these synergistic effects optimize ion selectivity and transport, rendering the composite an effective electrode for $NH_4^+$ ions [97–99]. Also, $NH_4^+$ exhibits a lower hydration energy (307 kJ $mol^{-1}$) in contrast to $Ca^{2+}$ (1577 kJ $mol^{-1}$) and $Na^+$ (406 kJ $mol^{-1}$). The selectivity of $NH_4^+$ over $Na^+$ and $Ca^{2+}$ is also attributed to its high affinity for N/O functional sites, the ion exchange with $H^+$ on these sites. $NH_4^+$ displaces $Na^+$ due to its stronger affinity for the N/O sites, while $Ca^{2+}$ experiences high charge repulsion and size effects that hinder its binding [100–102]. The micropores' enhancement was specifically tailored to accommodate $NH_4^+$ with its small hydrated radius (0.33 nm), effectively preventing the passage of larger hydrated $Ca^{2+}$ (0.41 nm) and $Na^+$ (0.36 nm) [103–105]. This heightened selectivity can be ascribed to the distinctive features introduced and ion mobility.

The RE and AEC of the FCDI method demonstrate its superiority over conventional technologies (Table 3). Traditional methods, such as microbial electrolysis cells (MEC) and microbial fuel cells (MFC), achieve removal efficiencies ranging from 70 to 90 %, with energy consumption of 5 to 12.4 kWh $kg^{-1}$ and 6 to 9.3 kWh $kg^{-1}$, respectively. The RO, adsorption, membrane bioreactor, and biological treatment methods show significant removal efficiency but are energy-intensive. The high energy consumption in these technologies, like RO, adsorption, membrane bioreactor, and biological treatment for ammonium removal, is due to their complex processes. These methods typically demand substantial energy inputs to function effectively and attain desired removal levels. Factors such as aeration, pumping, and material regeneration further add to their energy consumption. In contrast, FCDI exhibits an impressive RE of 86.7 to 88.5 %, while consuming significantly less energy, at 0.59 to 0.62 kWh $kg^{-1}$. This stark difference highlights FCDI's potential for more sustainable and cost-effective $NH_4^+$ removal from aqueous solutions, effectively outpacing traditional methods in both performance and efficiency.

**Table 3**
Energy consumption comparison between traditional and FCDI methods.

| Technology used | Removal efficiency (%) | Energy consumption (kWh $kg^{-1}$) | References |
|---|---|---|---|
| Microbial electrolysis cell (MEC) | 70–90 | 5–12.4 | [106] |
| Microbial fuel cell (MFC) | – | 10.93 | [107] |
| Ammonia stripping | 50–90 | 6–9 | [108] |
| Bipolar electrodialysis | ~90 | 5–20.4 | [109] |
| Ion exchange | ~87 | <1 | [110] |
| Battery electrode deionization (BDI) | >90 | 1.5–2.0 | [111] |
| Adsorption | 70–99 | 2–3 | [112] |
| Reverse osmosis (RO) | 85–98 | 40–120 | [113] |
| Biological treatment | 50–90 | 4.2–30 | [108] |
| FCDI | 86.7 | 0.62 | This study |

Table 4 presents a comparison of the FCDI system utilizing OP-400@0.5 as the flow electrode with data from previous studies on $NH_4^+$ removal. The analysis showcased that OP-400@0.5 maintains an impressive RE of 86.7 % and an average $NH_4^+$ removal rate of 17.3 mg $m^{-2}$ $min^{-1}$, achieved with lower carbon content (2.5 wt%) and IEMs contact area (14.4 $cm^2$) in comparison to materials like Polyaniline, AC, $Ti_3C_2T_x$ Mxene, AC + Potassium dititanate, and Na-Zeolite. Moreover, OP-400@0.5 exhibited a notable RE with a modest AEC of 0.62 kWh $kg^{-1}$. In comparison, alternative materials displayed lower removal efficiencies ranging from 39.5 to 60 %, coupled with varying energy consumptions between 0.124 kWh $kg^{-1}$ and 0.58 kWh $kg^{-1}$. It is worth noting that PDMC achieved a removal efficiency of 87.3 %, albeit consuming a higher adsorption energy of 2.62 kWh $kg^{-1}$. These findings underscore the potential of OP-400@0.5 as a favorable candidate for prospective applications in the field.

## 4. Conclusion

The challenge posed by $NH_4^+$ in water, this has led to the examination of promising techniques such as FCDI for water treatment. Utilizing biomass waste to prepare FCDI electrode not only proves environmentally friendly but also offers a sustainable solution for waste conversion and repurposing. In this study, OP-400@0.5 emerged with good electrochemical properties, hydrophilicity, and the presence of oxygenated carbon bonds. The MgO modification introduced ion exchange sites and polarities, highlighting a specific surface area of 389.56 $m^2$ $g^{-1}$ and an average pore size of 1.86 nm, crucial for electrosorption, particularly for small hydrated ions like $NH_4^+$. In the FCDI experiments, conducted under an applied voltage of 1.2 V, with a 2.5 wt% carbon content, and a flow rate of 10 mL $min^{-1}$, OP-400@0.5 demonstrated superior performance. It achieved an impressive RE of 86.7 % while consuming low energy at 0.62 kWh $kg^{-1}$. In contrast, the unmodified biochar OP-400 achieved a removal efficiency of only 51.5 % with higher energy consumption at 1.65 kWh $kg^{-1}$.

Through cyclic experiments, OP-400@0.5 showcased consistent $NH_4^+$ removal over multiple cycles, with a slight decrease observed in later cycles. Additionally, this biochar displayed enhanced $NH_4^+$ removal even in the presence of common co-existing ions like $Na^+$ and $Ca^{2+}$ found in simulated municipal wastewater. Repurposing orange peel waste into biochar and modifying it with MgO proves to be a promising approach for efficient $NH_4^+$ removal, highlighting its potential for sustainable water treatment solutions. Addressing the challenge of $NH_4^+$ in water through FCDI techniques and the creation of biochar from biomass signifies a significant step towards sustainable water treatment processes.

## CRediT authorship contribution statement

**Gabriel Mwalusambo:** Writing – original draft, Methodology, Funding acquisition, Data curation, Conceptualization. **Bethwel Tarus:** Writing – review & editing, Supervision, Funding acquisition, Conceptualization. **Joyce Elisadiki:** Investigation, Formal analysis. **Moon Son:** Writing – review & editing, Resources, Investigation, Data curation. **Hoo Hugo Kim:** Writing – review & editing, Resources, Formal analysis, Data curation. **Yusufu A.C. Jande:** Writing – review & editing, Visualization,

**Table 4**
Operational parameters and FCDI performance from literatures.

| Concentration (mM) | Volume (mL) | Electrode | Contact area ($cm^2$) | Time (min) | Applied voltage (V) | Carbon content (wt %) | Flow rate (mL $min^{-1}$) | R (%) | AARR (mg $m^{-2}$ $min^{-1}$) | AEC (kWh $kg^{-1}$) | Reference |
|---|---|---|---|---|---|---|---|---|---|---|---|
| 10 | 100 | Polyaniline | 32 | 120 | 1.2 | 5 | 10 | 87.3 | 40.95 | 2.62 | [2,3] |
| 5 | 25 | AC + potassium dititanate | 18.6 | 60 | 1.2 | 5 | 10 | 65 | 10.16 | 3.2 | [13] |
| 10 | – | $Ti_3C_2T_x$ Mxene | – | 115 | 1.2 | 10 | – | 60 | – | 0.45 | [114] |
| 10 | 80 | AC | 18 | 600 | 1.2 | 4 | 8 | 53.1 | – | 0.124 | [115] |
| 11.11 | 180 | Na-Zeolite | 77 | 120 | 1.2 | 5 | NA | 39.5 | 18 | 0.58 | [15] |
| 3.78 | 50 | Orange peel | 14.4 | 120 | 1.2 | 2.5 | 10 | 86.7 | 17.3 | 0.62 | This study |

Supervision, Funding acquisition. **Tusekile Alfredy:** Writing – review & editing, Supervision, Resources, Funding acquisition, Formal analysis, Conceptualization.

## Declaration of Generative AI and AI-assisted technologies in the writing process

During the preparation of this work, the author(s) used "DeepSeek" and "Poe" in order to improve language and readability with caution. After using this tool/service, the author(s) reviewed and edited the content as needed and take(s) full responsibility for the content of the publication.

## Declaration of competing interest

The author confirms there is no personal or financial conflict of interest to declare regarding this work.

## Data availability

Data will be made available on request.

## Acknowledgment

The work was carried out with the financial support of the Carnegie Corporation of New York to the PASET Regional Scholarship and Innovation Fund (RSI) DOCTAS project, through the International Centre of Insect Physiology and Ecology (ICIPE) Grant Ref. G-22-59858 and Mwalimu Nyerere University of Agriculture and Technology (MNUAT) under the Higher Education for Economic Transformation Project (HEET).

## Appendix A. Supplementary data

Supplementary data to this article can be found online at https://doi.org/10.1016/j.desal.2025.119312.

## References

[1] A. Alkhaldi, A. Alsultan, K. Alsaikhan, R. Xie, J. Li, Z. Peng, Removal and recovery of ammonium and phosphate from wastewater using a redox flow deionization cell (RFDC), ACS ES&T Water 3 (4) (2023) 1182–1191, https://doi.org/10.1021/acsestwater.2c00644.
[2] Li, B. Liu, D. Fang, P. Zhang, F. Li, X. Qiu, X. Mo, K. Li, Polyaniline-derived mesoporous carbon electrode for selective and efficient ammonium removal with in a flow-electrode capacitive deionization system, J. Environ. Chem. Eng. 11 (5) (2023) 110857, https://doi.org/10.1016/j.jece.2023.110857.
[3] H. Li, Y. Wang, Y. Zhao, L. Wang, J. Feng, F. Sun, Efficient simultaneous phosphate and ammonia adsorption using magnesium-modified biochar beads and their recovery performance, J. Environ. Chem. Eng. 11 (5) (2023) 110875, https://doi.org/10.1016/j.jece.2023.110875.
[4] T.-X. Zhang, M.-R. Li, C. Liu, S.-P. Wang, Z.-G. Yan, A review of the toxic effects of ammonia on invertebrates in aquatic environments, Environ. Pollut. 336 (2023) 122374, https://doi.org/10.1016/j.envpol.2023.122374.
[5] J.H. Katonge, Status of livestock water quality and digestive upsets in Babati and Burunge areas, northern Tanzania, Eng. Sci. Technol. Int. J. 16 (1) (2024) 1–8, https://doi.org/10.4314/ijest.v16i1.1.
[6] M. Sheikh, J. Lopez, M. Reig, X. Vecino, M. Rezakazemi, C. Valderrama, J. Cortina, Ammonia recovery from municipal wastewater using hybrid NaOH closed-loop membrane contactor and ion exchange system, Chem. Eng. J. 465 (2023) 142859, https://doi.org/10.1016/j.cej.2023.142859.
[7] M.-H. Yuan, Y.-H. Chen, J.-Y. Tsai, C.-Y. Chang, Ammonia removal from ammonia-rich wastewater by air stripping using a rotating packed bed, Process. Saf. Environ. Prot. 102 (2016) 777–785, https://doi.org/10.1016/j.psep.2016.06.021.
[8] T. Alfredy, J. Elisadiki, Y.-D. Kim, Y.A.C. Jande, Water defluoridation using Al/Fe/Ti ternary metal oxide-loaded activated carbon by capacitive deionization, Environ. Sci. Water Res. Technol. 9 (3) (2023) 957–972, https://doi.org/10.1039/D2EW00614F.
[9] J. Elisadiki, T.E. Kibona, R.L. Machunda, M.W. Saleem, W.-S. Kim, Y.A. Jande, Biomass-based carbon electrode materials for capacitive deionization: a review, Biomass Convers. Biorefinery 10 (2020) 1327–1356, https://doi.org/10.1007/s13399-019-00463-9.
[10] K. Fang, H. Gong, W. He, F. Peng, C. He, K. Wang, Recovering ammonia from municipal wastewater by flow-electrode capacitive deionization, Chem. Eng. J. 348 (2018) 301–309, https://doi.org/10.1016/j.cej.2018.04.128.
[11] Y. Dong, W. Xing, K. Luo, J. Zhang, J. Yu, W. Jin, J. Wang, W. Tang, Effective and continuous removal of Cr (VI) from brackish wastewater by flow-electrode capacitive deionization (FCDI), J. Clean. Prod. 326 (2021) 129417, https://doi.org/10.1016/j.jclepro.2021.129417.
[12] M.M. Elewa, M. El Batouti, N.F. Al-Harby, A comparison of capacitive deionization and membrane capacitive deionization using novel fabricated ion exchange membranes, Materials 16 (13) (2023) 4872, https://doi.org/10.3390/ma16134872.
[13] L. Lin, J. Hu, J. Liu, X. He, B. Li, X.-y. Li, Selective ammonium removal from synthetic wastewater by flow-electrode capacitive deionization using a novel K2Ti2O5-activated carbon mixture electrode, Environ. Sci. Technol. 54 (19) (2020) 12723–12731, https://doi.org/10.1021/acs.est.0c04383.
[14] C. Zhang, J. Ma, L. Wu, J. Sun, L. Wang, T. Li, T.D. Waite, Flow electrode capacitive deionization (FCDI): recent developments, environmental applications, and future perspectives, Environ. Sci. Technol. 55 (8) (2021) 4243–4267, https://doi.org/10.1021/acs.est.0c06552.
[15] X. He, W. Chen, F. Sun, Z. Jiang, B. Li, X.-y. Li, L. Lin, Enhanced NH4+ removal and recovery from wastewater using Na-zeolite-based flow-electrode capacitive deionization: insight from ion transport flux, Environ. Sci. Technol. 57 (23) (2023) 8828–8838, https://doi.org/10.1021/acs.est.3c02286.
[16] M. Tauk, P. Sistat, R. Habchi, M. Cretin, F. Zaviska, M. Bechelany, Exploring flow-electrode capacitive deionization: an overview and new insights, Desalination (2024) 118392, https://doi.org/10.1016/j.desal.2024.118392.
[17] T. Chen, L. Xu, S. Wei, Z. Fan, R. Qian, X. Ren, G. Zhou, H. Yang, J. Wu, H. Chen, Ammonia-rich solution production from coal gasification gray water using chemical-free flow-electrode capacitive deionization coupled with a monovalent cation exchange membrane, Chem. Eng. J. 433 (2022) 133780, https://doi.org/10.1016/j.cej.2021.133780.
[18] Y.-X. Jiang, W.-C. Zhang, Y.-M. Deng, J.-X. Cao, J.A. Asare, S.I. Alhassan, F.-L. Zhang, P. Wang, H.-Y. Wang, The electrode materials in flow-electrode capacitive deionization desalination: a mini review, Rare Metals (2025) 1–20, https://doi.org/10.1007/s12598-024-03215-5.
[19] H. Liu, L. Zhang, J. Cai, S. Liu, C. Zhao, S. Wang, M. Zhao, M. Liu, W. Ding, H. Zhou, Biomass-derived nitrogen-doped porous carbon as a sustainable flow-electrode material for enhanced capacitive deionization, Chin. J. Chem. Eng. (2025), https://doi.org/10.1016/j.cjche.2025.04.001.
[20] M. Mariana, A.K. Hps, E. Mistar, E.B. Yahya, T. Alfatah, M. Danish, M. Amayreh, Recent advances in activated carbon modification techniques for enhanced heavy metal adsorption, J. Water Process Eng. 43 (2021) 102221, https://doi.org/10.1016/j.jwpe.2021.102221.
[21] V.I. Isaeva, M.D. Vedenyapina, A.Y. Kurmysheva, D. Weichgrebe, R.R. Nair, N.P. T. Nguyen, L.M. Kustov, Modern carbon–based materials for adsorptive removal of organic and inorganic pollutants from water and wastewater, Molecules 26 (21) (2021) 6628, https://doi.org/10.3390/molecules26216628.

[22] M.M. Sabzehmeidani, S. Mahnaee, M. Ghaedi, H. Heidari, V.A. Roy, Carbon based materials: a review of adsorbents for inorganic and organic compounds, Mater. Adv. 2 (2) (2021) 598–627, https://doi.org/10.1039/D0MA00087F.
[23] H. Lyu, X.-G. Sun, S. Dai, Organic cathode materials for lithium-ion batteries: past, present, and future, Adv. Energy Sustain. Res. 2 (1) (2021) 2000044, https://doi.org/10.1002/aesr.202000044.
[24] H. Qiu, M. Shi, P. Zhang, Y. Tao, X. Zhang, J. Yang, J. Zhao, H. Pang, An electron-delocalized sp 2-N hybridized organic electrode enables sustainable and high-efficiency electrochemical ammonium removal, Chem. Sci. 16 (22) (2025) 9895–9904, https://doi.org/10.1039/D5SC02192H.
[25] D. Chen, Y. Yin, Y. Xu, C. Liu, Adsorptive recycle of phosphate by MgO-biochar from wastewater: adsorbent fabrication, adsorption site energy analysis and long-term column experiments, J. Water Process Eng. 51 (2023) 103445, https://doi.org/10.1016/j.jwpe.2022.103445.
[26] R.B. Kalengyo, M.G. Ibrahim, M. Fujii, M. Nasr, Utilizing orange peel waste biomass in textile wastewater treatment and its recyclability for dual biogas and biochar production: a techno-economic sustainable approach, Biomass Convers. Biorefinery 14 (16) (2024) 19875–19888, https://doi.org/10.1007/s13399-023-04111-1.
[27] H. Wang, X. Zhang, X. Li, Y. Li, D. Kong, Z. Zhen, L. Geng, L. Zhi, Z. Li, Hierarchically porous biomass carbon derived from orange peel for atomically dispersed Co-NC sites toward advanced oxygen reduction reaction, Renewables 1 (3) (2023) 353–361, https://doi.org/10.31635/renewables.023.202200017.
[28] V. Negro, B. Ruggeri, D. Fino, D. Tonini, Life cycle assessment of orange peel waste management, Resour. Conserv. Recycl. 127 (2017) 148–158, https://doi.org/10.1016/j.resconrec.2017.08.014.
[29] W. Zhang, Y. Wang, L. Fan, X. Liu, W. Cao, H. Ai, Z. Wang, X. Liu, H. Jia, Sorbent properties of orange peel-based biochar for different pollutants in water, Processes 10 (5) (2022) 856, https://doi.org/10.3390/pr10050856.
[30] J.K. Bediako, S. Lin, A.K. Sarkar, Y. Zhao, J.-W. Choi, M.-H. Song, C.-W. Cho, Y.-S. Yun, Evaluation of orange peel-derived activated carbons for treatment of dye-contaminated wastewater tailings, Environ. Sci. Pollut. Res. 27 (2020) 1053–1068, https://doi.org/10.1007/s11356-019-07031-8.
[31] Z. Chen, B. Lin, Y. Huang, Y. Liu, Y. Wu, R. Qu, C. Tang, Pyrolysis temperature affects the physiochemical characteristics of lanthanum-modified biochar derived from orange peels: insights into the mechanisms of tetracycline adsorption by spectroscopic analysis and theoretical calculations, Sci. Total Environ. 862 (2023) 160860, https://doi.org/10.1016/j.scitotenv.2022.160860.
[32] S. Zhengfeng, C. Ming, W. Geming, D. Quanrong, W. Shenggao, G. Yuan, Synthesis, characterization and removal performance of Cr (VI) by orange peel-based activated porous biochar from water, Chem. Eng. Res. Des. 193 (2023) 1–12, https://doi.org/10.1016/j.cherd.2023.03.011.
[33] A. Li, W. Ge, L. Liu, G. Qiu, Preparation, adsorption performance and mechanism of MgO-loaded biochar in wastewater treatment: a review, Environ. Res. 212 (2022) 113341, https://doi.org/10.1016/j.envres.2022.113341.
[34] J. Yang, Q. Wei, C. Tian, D. Li, H. Li, G. Qin, K. Hu, Q. Zhang, Preparation of biomass carbon composites MgO@ ZnO@ BC and its adsorption and removal of cu (II) and Pb (II) in wastewater, Molecules 28 (19) (2023) 6982, https://doi.org/10.3390/molecules28196982.
[35] R. Ahuja, A. Kalia, R. Sikka, C. P, Nano modifications of biochar to enhance heavy metal adsorption from wastewaters: a review, ACS Omega 7 (50) (2022) 45825–45836, https://doi.org/10.1021/acsomega.2c05117.
[36] D. Bao, Z. Li, R. Tang, C. Wan, C. Zhang, X. Tan, X. Liu, Metal-modified sludge-based biochar enhance catalytic capacity: characteristics and mechanism, J. Environ. Manag. 284 (2021) 112113, https://doi.org/10.1016/j.jenvman.2021.112113.
[37] S.P. Mishra, Insights into the recent use of modified adsorbents in removing heavy metal ions from aqueous solution, Biointerface Res. Appl. Chem. 12 (2021) 1884–1898, https://doi.org/10.33263/BRIAC122.18841898.
[38] Y.-E. Lee, Y. Jeong, D.-C. Shin, K.-H. Ahn, J.-H. Jung, I.-T. Kim, Fabrication of mg-doped sargassum biochar for phosphate and ammonium recovery, Sustainability 13 (22) (2021) 12752, https://doi.org/10.3390/su132212752.
[39] P. Zhou, Y. Shen, S. Zhao, Y. Chen, S. Gao, W. Liu, D. Wei, Hydrothermal synthesis of novel ternary hierarchical MoS2/TiO2/clinoptilolite nanocomposites with remarkably enhanced visible light response towards xanthates, Appl. Surf. Sci. 542 (2021) 148578, https://doi.org/10.1016/j.apsusc.2020.148578.
[40] Y.-J. Heo, S.-J. Park, Facile synthesis of MgO-modified carbon adsorbents with microwave-assisted methods: effect of MgO particles and porosities on CO2 capture, Sci. Rep. 7 (1) (2017) 5653, https://doi.org/10.1038/s41598-017-06091-5.
[41] T.K. Enock, C.K. King'ondu, A. Pogrebnoi, Y.A.C. Jande, Biogas-slurry derived mesoporous carbon for supercapacitor applications, Materials Today Energy 5 (2017) 126–137.
[42] C. Zhang, D. He, J. Ma, W. Tang, T.D. Waite, Faradaic reactions in capacitive deionization (CDI)-problems and possibilities: a review, Water Res. 128 (2018) 314–330, https://doi.org/10.1016/j.watres.2017.10.024.
[43] H.M. Saif, B. Ferrández-Gómez, V.D. Alves, R.M. Huertas, G. Alemany-Molina, A. Viegas, E. Morallón, D. Cazorla-Amorós, J.G. Crespo, S. Pawlowski, Activated carbons for flow electrode capacitive deionization (FCDI) – morphological, electrochemical and rheological analysis, Desalination 602 (2025) 118638, https://doi.org/10.1016/j.desal.2025.118638.
[44] K. Karthikeyan, S. Amaresh, V. Aravindan, Y. Lee, Microwave assisted green synthesis of MgO–carbon nanotube composites as electrode material for high power and energy density supercapacitors, J. Magn. Reson. 1 (12) (2013) 4105–4111, https://doi.org/10.1039/C3TA01608K.
[45] S.S. Chen, Y. Cao, D.C. Tsang, J.-P. Tessonnier, J. Shang, D. Hou, Z. Shen, S. Zhang, Y.S. Ok, K.C.-W. Wu, Effective dispersion of MgO nanostructure on biochar support as a basic catalyst for glucose isomerization, ACS Sustain. Chem. Eng. 8 (18) (2020) 6990–7001, https://doi.org/10.1021/acssuschemeng.0c00278.
[46] L. Hu, R. Huang, L. Zhou, R. Qin, X. He, H. Deng, K. Li, Effects of magnesium-modified biochar on soil organic carbon mineralization in citrus orchard, Front. Microbiol. 14 (2023) 1109272, https://doi.org/10.3389/fmicb.2023.1109272.
[47] N. Kasera, D. Paul, P. Kolar, S.G. Hall, S. Adhikari, M. Sarker, A. Sinitskii, Synthesis, Characterization, and Use of Magnesium-activated Biochar for Nitrate Removal From Aqueous Solutions, 2024, https://doi.org/10.21203/rs.3.rs-4802237/v1.
[48] Y. Zheng, Y. Wan, J. Chen, H. Chen, B. Gao, MgO modified biochar produced through ball milling: a dual-functional adsorbent for removal of different contaminants, Chemosphere 243 (2020) 125344, https://doi.org/10.1016/j.chemosphere.2019.125344.
[49] V.V. Pattanshetti, G. Shashidhara, M.G. Veena, Dielectric and thermal properties of magnesium oxide/poly (aryl ether ketone) nanocomposites, Sci. Eng. Compos. Mater. 25 (5) (2018) 915–925, https://doi.org/10.1515/secm-2016-0273.
[50] X. An, Z. Wu, J. Yu, L. Ge, T. Li, X. Liu, B. Yu, High-efficiency reclaiming phosphate from an aqueous solution by bentonite modified biochars: a slow release fertilizer with a precise rate regulation, ACS Sustain. Chem. Eng. 8 (15) (2020) 6090–6099, https://doi.org/10.1021/acssuschemeng.0c01112.
[51] X. Zhang, Y. Xiong, X. Wang, Z. Wen, X. Xu, J. Cui, Z. Liu, L. Wei, X. An, MgO-modified biochar by modifying hydroxyl and amino groups for selective phosphate removal: insight into phosphate selectivity adsorption mechanism through experimental and theoretical, Sci. Total Environ. 918 (2024) 170571, https://doi.org/10.1016/j.scitotenv.2024.170571.
[52] K.M. George, T.C. Ruthenburg, J. Smith, L. Yu, Q. Zhang, C. Anastasio, A. M. Dillner, FT-IR quantification of the carbonyl functional group in aqueous-phase secondary organic aerosol from phenols, Atmos. Environ. 100 (2015) 230–237, https://doi.org/10.1016/j.atmosenv.2014.11.011.
[53] S. Purwajanti, X. Huang, Y. Liu, Y. Yang, O. Noonan, H. Song, J. Zhang, J. Zhang, J. Fu, C. Liang, Mg (OH) 2–MgO@ reduced graphene oxide nanocomposites: the roles of composition and nanostructure in arsenite sorption, J. Mater. Chem. A 5 (46) (2017) 24484–24492, https://doi.org/10.1039/C7TA07629K.
[54] A. Abdelaal, S. Pradhan, A. AlNouss, Y. Tong, T. Al-Ansari, G. McKay, H. R. Mackey, The impact of pyrolysis conditions on orange peel biochar physicochemical properties for sandy soil, Waste Manag. Res. 39 (7) (2021) 995–1004, https://doi.org/10.1177/0734242X20978456.
[55] S. Xu, D. Li, H. Guo, H. Lu, M. Qiu, J. Yang, F. Shen, Solvent-free synthesis of MgO-modified biochars for phosphorus removal from wastewater, Int. J. Environ. Res. Public Health 19 (13) (2022) 7770, https://doi.org/10.3390/ijerph19137770.
[56] A. Pedico, S. Bocchini, E. Tresso, A. Lamberti, Enhanced capacitive deionization exploiting novel functionalized graphene oxide electrodes, Adv. Mater. Technol. 7 (8) (2022) 2101513, https://doi.org/10.1002/admt.202101513.
[57] J.W. Suen, N.K. Elumalai, S. Debnath, N.M. Mubarak, C.I. Lim, M. Reddy Moola, Y.S. Tan, M. Khalid, Investigating the correlation between electrolyte concentration and electrochemical properties of ionogels, Molecules 28 (13) (2023) 5192, https://doi.org/10.3390/molecules28135192.
[58] E. Baba, G. Wyasu, A.J. Adefila, N.A. Dikko, J.B. Yakasa, Production and characterization of activated carbon derived from orange peel for the adsorption of methylene blue dye, Sci. World J. 18 (3) (2023) 492–498, https://doi.org/10.4314/swj.v18i3.25.
[59] R.S. Salama, M.S. Gouda, M.F.A. Aboud, F.T. Alshorifi, A. El-Hallag, A.K. Badawi, Synthesis and characterization of magnesium ferrite-activated carbon composites derived from orange peels for enhanced supercapacitor performance, Sci. Rep. 14 (1) (2024) 8223, https://doi.org/10.1038/s41598-024-60087-6.
[60] L. Liu, B. Feng, Y.Z. Rao, C.S. Tian, Q.X. Gu, T. Huang, Development of efficient biochar produced from orange peel for effective La (III) and Y (III) adsorption, Adsorpt. Sci. Technol. 2023 (2023) 5519783, https://doi.org/10.1155/2023/55197.
[61] Y. Lv, L. Bai, Y. Ma, L. Zhao, Investigation of crystallization growth characteristics of Mg (OH) 2 crystals under unconstrained conditions, Materials 17 (9) (2024) 1956, https://doi.org/10.3390/ma17091956.
[62] E. Panja, T. Alfredy, J. Elisadiki, Y.A. Jande, *Hermetia illucens* pupae casings and biogas slurry activated carbon electrodes for Cd2+ removal from aqueous solutions using capacitive deionization, Desalin. Water Treat. (2025) 101118, https://doi.org/10.1016/j.dwt.2025.101118.
[63] P.S. Kumar, L. Korving, K.J. Keesman, M.C. van Loosdrecht, G.-J. Witkamp, Effect of pore size distribution and particle size of porous metal oxides on phosphate adsorption capacity and kinetics, Chem. Eng. J. 358 (2019) 160–169, https://doi.org/10.1016/j.cej.2018.09.202.
[64] M. Dhelipan, A. Arunchander, A. Sahu, D. Kalpana, Activated carbon from orange peels as supercapacitor electrode and catalyst support for oxygen reduction reaction in proton exchange membrane fuel cell, J. Saudi Chem. Soc. 21 (4) (2017) 487–494, https://doi.org/10.1016/j.jscs.2016.12.003.
[65] A. Kolganova, R. Lal, J. Firkins, Biochar's electrochemical properties impact on methanogenesis: ruminal vs. soil processes, J. Agric. Chem. Environ. 12 (1) (2023) 28–43, https://doi.org/10.4236/jacen.2023.121003.
[66] A. Schievano, R. Berenguer, A. Goglio, S. Bocchi, S. Marzorati, L. Rago, R. O. Louro, C.M. Paquete, A. Esteve-Núñez, Electroactive biochar for large-scale environmental applications of microbial electrochemistry, ACS Sustain. Chem. Eng. 7 (22) (2019) 18198–18212, https://doi.org/10.1021/acssuschemeng.9b04229.

[67] G. Kharel, O. Sacko, X. Feng, J.R. Morris, C.L. Phillips, K. Trippe, S. Kumar, J. W. Lee, Biochar surface oxygenation by ozonization for super high cation exchange capacity, ACS Sustain. Chem. Eng. 7 (19) (2019) 16410–16418, https://doi.org/10.1021/acssuschemeng.9b03536.
[68] C. Nzediegwu, M.A. Naeth, S.X. Chang, Elemental composition of biochars is affected by methods used for its determination, J. Anal. Appl. Pyrolysis 156 (2021) 105174, https://doi.org/10.1016/j.jaap.2021.105174.
[69] K. Tian, J. Wang, L. Cao, W. Yang, W. Guo, S. Liu, W. Li, F. Wang, X. Li, Z. Xu, Single-site pyrrolic-nitrogen-doped sp 2-hybridized carbon materials and their pseudocapacitance, Nat. Commun. 11 (1) (2020) 3884, https://doi.org/10.1038/s41467-020-17727-y.
[70] X. Ning, Y. Li, J. Ming, Q. Wang, H. Wang, Y. Cao, F. Peng, Y. Yang, H. Yu, Electronic synergism of pyridinic-and graphitic-nitrogen on N-doped carbons for the oxygen reduction reaction, Chem. Sci. 10 (6) (2019) 1589–1596, https://doi.org/10.1039/C8SC04596H.
[71] J. Wu, L. Ma, R.M. Yadav, Y. Yang, X. Zhang, R. Vajtai, J. Lou, P.M. Ajayan, Nitrogen-doped graphene with pyridinic dominance as a highly active and stable electrocatalyst for oxygen reduction, ACS Appl. Mater. Interfaces 7 (27) (2015) 14763–14769, https://doi.org/10.1021/acsami.5b02902.
[72] G. Hegde, S.A. Abdul Manaf, A. Kumar, G.A. Ali, K.F. Chong, Z. Ngaini, K. Sharma, Biowaste sago bark based catalyst free carbon nanospheres: waste to wealth approach, ACS Sustain. Chem. Eng. 3 (9) (2015) 2247–2253, https://doi.org/10.1021/acssuschemeng.5b00517.
[73] I.I. Misnon, N.K.M. Zain, R. Abd Aziz, B. Vidyadharan, R. Jose, Electrochemical properties of carbon from oil palm kernel shell for high performance supercapacitors, Electrochim. Acta 174 (2015) 78–86, https://doi.org/10.1016/j.electacta.2015.05.163.
[74] C. Ranaweera, P. Kahol, M. Ghimire, S. Mishra, R.K. Gupta, Orange-peel-derived carbon: designing sustainable and high-performance supercapacitor electrodes, C 3 (3) (2017) 25, https://doi.org/10.3390/c3030025.
[75] J. Cheng, Y. Lu, Y. Sun, S. Deng, H. Yang, M. Zhang, C. Wang, J. Yan, Impact of activation conditions on the electrochemical performance of rice straw biochar for supercapacitor electrodes, Molecules 30 (3) (2025) 632, https://doi.org/10.3390/molecules30030632.
[76] G. Simoes dos Reis, C. Mayandi Subramaniyam, A.D. Cárdenas, S.H. Larsson, M. Thyrel, U. Lassi, F. Garcia-Alvarado, Facile synthesis of sustainable activated biochars with different pore structures as efficient additive-carbon-free anodes for lithium-and sodium-ion batteries, ACS Omega 7 (46) (2022) 42570–42581, https://doi.org/10.1021/acsomega.2c06054.
[77] O. Sufiani, H. Tanaka, K. Teshima, R.L. Machunda, Y.A. Jande, Enhanced electrosorption capacity of activated carbon electrodes for deionized water production through capacitive deionization, Sep. Purif. Technol. 247 (2020) 116998, https://doi.org/10.1016/j.seppur.2020.116998.
[78] Y. Tao, Y. Cui, H. Wang, Z. Li, Z. Qian, P. Zhang, H. Zhou, M. Shi, High-efficiency electrochemical desalination: the role of a rigid pseudocapacitive polymer electrode with diverse active sites, Adv. Funct. Mater. 35 (6) (2025) 2414805, https://doi.org/10.1002/adfm.202414805.
[79] J. Yang, Y. Tao, C. Zhao, Y. Cai, P. Xiao, M. Shi, Tailorable dual-redox polymer with molecular flexibility for enhanced electrochemical desalination and water purification, Environ. Sci. Technol. 59 (22) (2025) 10980–10989, https://doi.org/10.1021/acs.est.5c04042.
[80] Y. Cui, Y. Tao, J. Yang, H. Wang, P. Zhang, G. Li, M. Shi, E.H. Ang, A ladder-type organic molecule with pseudocapacitive properties enabling superior electrochemical desalination, Mater. Horiz. (2025), https://doi.org/10.1039/D4MH01342E.
[81] A. Dieguez-Alonso, A. Funke, A. Anca-Couce, A.G. Rombolà, G. Ojeda, J. Bachmann, F. Behrendt, Towards biochar and hydrochar engineering—influence of process conditions on surface physical and chemical properties, thermal stability, nutrient availability, toxicity and wettability, Energies 11 (3) (2018) 496, https://doi.org/10.3390/en11030496.
[82] J. Lim, Y.-U. Shin, S. Hong, Enhanced capacitive deionization using a biochar-integrated novel flow-electrode, Desalination 528 (2022) 115636, https://doi.org/10.1016/j.desal.2022.115636.
[83] H. Gu, C. Hou, Y. Mao, D. Wu, Navigating the dual pathways of ion removal in flow-electrode capacitive deionization: capacitive trapping vs. electrodialytic migration, Chem. Eng. J. (2025), https://doi.org/10.1016/j.cej.2025.165294.
[84] S. Mai, H. Huang, J. Long, Y. Deng, H. Zhang, Y. Xie, H. Li, Enhanced simultaneous removal of thallium and cadmium using flow-electrode capacitive deionization, J. Environ. Chem. Eng. (2025) 116938.
[85] M. Tan, Y. Li, D. Chi, Q. Wu, Efficient removal of ammonium in aqueous solution by ultrasonic magnesium-modified biochar, Chem. Eng. J. 461 (2023) 142072, https://doi.org/10.1016/j.cej.2023.142072.
[86] E.E.C. Kurz, U. Hellriegel, V.T. Luong, J. Bundschuh, J. Hoinkis, Selective ion adsorption with pilot-scale membrane capacitive deionization (MCDI): arsenic, ammonium, and manganese removal, Desalin. Water Treat. 198 (2020) 163–169, https://doi.org/10.5004/dwt.2020.26036.
[87] C. Zhang, J. Ma, T.D. Waite, Ammonia-rich solution production from wastewaters using chemical-free flow-electrode capacitive deionization, ACS Sustain. Chem. Eng. 7 (7) (2019) 6480–6485, https://doi.org/10.1021/acssuschemeng.9b00314.
[88] K. Alsaikhan, A. Alsultan, A. Alkhaldi, A. Bentalib, A. Abutalib, D. Wu, J. Li, R. Xie, Z. Peng, Carbon material-based flow-electrode capacitive deionization for continuous water desalination, Processes 11 (1) (2023) 195, https://doi.org/10.3390/pr11010195.
[89] P. Ren, B. Wang, J.G. de Andrade Ruthes, M. Torkamanzadeh, V. Presser, Cation selectivity during flow electrode capacitive deionization, Desalination 592 (2024) 118161, https://doi.org/10.1016/j.desal.2024.118161.
[90] J. Ma, C. He, D. He, C. Zhang, T.D. Waite, Analysis of capacitive and electrodialytic contributions to water desalination by flow-electrode CDI, Water Res. 144 (2018) 296–303, https://doi.org/10.1016/j.watres.2018.07.049.
[91] N. Bernárdez-Rodas, E. Rosales, M. Pazos, Ó. González-Prieto, L.O. Torres, M.Á. Sanromán, Three-dimensional Electrosorption for pharmaceutical wastewater management and sustainable biochar regeneration, Molecules 30 (7) (2025) 1435, https://doi.org/10.3390/molecules30071435.
[92] O. Pastushok, D.L. Ramasamy, M. Sillanpää, E. Repo, Enhanced ammonium removal and recovery from municipal wastewater by asymmetric CDI cell equipped with oxygen functionalized carbon electrode, Sep. Purif. Technol. 274 (2021) 119064, https://doi.org/10.1016/j.seppur.2021.119064.
[93] H. Stephanie, T.E. Mlsna, D.O. Wipf, Functionalized biochar electrodes for asymmetrical capacitive deionization, Desalination 516 (2021) 115240, https://doi.org/10.1016/j.desal.2021.115240.
[94] Y. Zhang, X. Bu, Y. Wang, Z. Hang, Z. Chen, Hierarchically porous biochar derived from aerobic granular sludge for high-performance membrane capacitive deionization, Environ. Sci. Ecotechnol. 17 (2024) 100297, https://doi.org/10.1016/j.ese.2023.100297.
[95] C. Wang, S. Adhikari, Y. Li, M. Wen, Y. Wang, Highly selective zinc ion removal by the synergism of functional groups and defects from N, S co-doped biochar, Sep. Purif. Technol. 354 (2025) 129446, https://doi.org/10.1016/j.seppur.2024.129446.
[96] C. Wang, Y. Li, Y. Qiao, N.L. Tut, D. Deng, Q. Pan, G. Yao, Y. Wang, The regulation of biochar surface potential to achieve rapid capacitive deionization, J. Environ. Chem. Eng. 11 (6) (2023) 111560, https://doi.org/10.1016/j.jece.2023.111560.
[97] J.E. Lee, Y.-K. Park, Applications of modified biochar-based materials for the removal of environment pollutants: a mini review, Sustainability 12 (15) (2020) 6112, https://doi.org/10.3390/su12156112.
[98] Y. Li, C. Wang, D. Deng, Y. Qiao, G. Yao, Y. Wang, Asymmetric capacitive deionization based on pore structures of biochar, Desalination 583 (2024) 117675, https://doi.org/10.1016/j.desal.2024.117675.
[99] H. Tan, C.T. Lee, K.Y. Wong, P.Y. Ong, M.H.D. Othman, K.S. Woon, G.R. Mong, Comparison between chemical modification of biochar for different environmental applications, Chem. Eng. Trans. 114 (2024) 535–540, https://doi.org/10.3303/CET24114090.
[100] J. Gamaethiralalage, J. Muff, L.C. de Smet, Effect of dopants in polyaniline-coated capacitive deionization electrodes on anion selectivity, Prog. Org. Coat. 197 (2024) 108854, https://doi.org/10.1016/j.porgcoat.2024.108854.
[101] H. Lin, D. Yang, C. Zhang, W. Liu, L. Zhang, Y. Dong, Selective removal behavior of lead and cadmium from calcium-rich solution by MgO loaded soybean straw biochars and mechanism analysis, Chemosphere 319 (2023) 138010, https://doi.org/10.1016/j.chemosphere.2023.138010.
[102] L. Luo, H.Q. Yu, Coexisting ion concentration polarization in ammonia recovery via flow-electrode CDI: impacts, mechanisms, and optimizations, Environ. Sci. Technol. 59 (25) (2025) 13054–13062, https://doi.org/10.1021/acs.est.5c02340.
[103] K. Jindo, H. Mizumoto, Y. Sawada, M.A. Sanchez-Monedero, T. Sonoki, Physical and chemical characterization of biochars derived from different agricultural residues, Biogeosciences 11 (23) (2014) 6613–6621, https://doi.org/10.5194/bg-11-6613-2014.
[104] S. Wang, H. Zhao, J. Liu, X. Wang, J. Li, E. Shi, C. Wang, J. Yang, Z. Zhang, A study on and adsorption mechanism of ammonium nitrogen by modified corn straw biochar, R. Soc. Open Sci. 10 (2) (2023) 221535, https://doi.org/10.1098/rsos.221535.
[105] R. Xiao, H. Zhang, Z. Tu, R. Li, S. Li, Z. Xu, Z. Zhang, Enhanced removal of phosphate and ammonium by MgO-biochar composites with NH 3· H 2 O hydrolysis pretreatment, Environ. Sci. Pollut. Res. 27 (2020) 7493–7503, https://doi.org/10.1007/s11356-019-07355-5.
[106] S.A. Hussain, M. Perrier, B. Tartakovsky, Long-term performance of a microbial electrolysis cell operated with periodic disconnection of power supply, RSC Adv. 8 (30) (2018) 16842–16849, https://doi.org/10.1039/C8RA01863D.
[107] P. Kuntke, K. Śmiech, H. Bruning, G. Zeeman, M. Saakes, T. Sleutels, H. Hamelers, C. Buisman, Ammonium recovery and energy production from urine by a microbial fuel cell, Water Res. 46 (8) (2012) 2627–2636, https://doi.org/10.1016/j.watres.2012.02.025.
[108] P. Ochs, B. Martin, E. Germain-Cripps, T. Stephenson, M. van Loosdrecht, A. Soares, Techno-economic analysis of sidestream ammonia removal technologies: biological options versus thermal stripping, Environ. Sci. Ecotechnol. 13 (2023) 100220, https://doi.org/10.1016/j.ese.2022.100220.
[109] T.-L. Chen, L.-H. Chen, Y.J. Lin, C.-P. Yu, H.-w. Ma, P.-C. Chiang, Advanced ammonia nitrogen removal and recovery technology using electrokinetic and stripping process towards a sustainable nitrogen cycle: a review, J. Clean. Prod. 309 (2021) 127369, https://doi.org/10.1016/j.jclepro.2021.127369.
[110] J. Huang, N.R. Kankanamge, C. Chow, D.T. Welsh, T. Li, P.R. Teasdale, Removing ammonium from water and wastewater using cost-effective adsorbents: a review, J. Environ. Sci. 63 (2018) 174–197, https://doi.org/10.1016/j.jes.2017.09.009.
[111] M. Son, B.L. Aronson, W. Yang, C.A. Gorski, B.E. Logan, Recovery of ammonium and phosphate using battery deionization in a background electrolyte, Environ. Sci. Water Res. Technol. 6 (6) (2020) 1688–1696, https://doi.org/10.1039/D0EW00183J.
[112] V. Gupta, H. Sadegh, M. Yari, G.R. Shahryari, B. Maazinejad, M. Chahardori, Removal of ammonium ions from wastewater a short review in development of efficient methods, Glob. J. Environ. Sci. Manage. 1 (2) (2015) 149–158. https://sid.ir/paper/343370/en.

[113] H. Chang, M. Lu, Y. Zhu, Z. Zhang, Z. Zhou, Y. Liang, R.D. Vidic, Consideration of potential technologies for ammonia removal and recovery from produced water, Environ. Sci. Technol. 56 (6) (2022) 3305–3308, https://doi.org/10.1021/acs.est.1c08517.

[114] N.E. Mansoor, L.A. Diaz, C.E. Shuck, Y. Gogotsi, T.E. Lister, D. Estrada, Removal and recovery of ammonia from simulated wastewater using Ti3C2T x MXene in flow electrode capacitive deionization, NPJ Clean Water 5 (1) (2022) 26, https://doi.org/10.1038/s41545-022-00164-3.

[115] H. Sun, X. Zhang, M. Cui, G. Liu, H. Liu, S. Huang, D.S. Ghasimi, H. Liu, Separation of nutrients and acetate from sewage sludge fermentation liquid in flow-electrode capacitive deionization system: competitive mechanisms of ions and influence of activated carbon, Bioresour. Technol. 390 (2023) 129864, https://doi.org/10.1016/j.biortech.2023.129864.